Pursuit of quantum monodromy in the far-infrared and mid-infrared spectra of NCNCS using synchrotron radiation

Journal:	*Physical Chemistry Chemical Physics*
Manuscript ID:	CP-PER-04-2014-001443
Article Type:	Perspective
Date Submitted by the Author:	08-Apr-2014
Complete List of Authors:	Winnewisser, Manfred; The Ohio State University, Department of Physics Winnewisser, Brenda; The Ohio State University, Department of Physics De Lucia, Frank C; The Ohio State University, Department of Physics Tokaryk, Dennis; University of New Brunswick, Department of Physics and Centre for Laser, Atomic, and Molecular Sciences Ross, Stephen; University of New Brunswick, Physics Billinghurst, Brant; Candian Light Source,

Draft of our PCCP Perspective Manuscript; For Your Eyes Only: Pursuit of quantum monodromy in the far-infrared and mid-infrared spectra of NCNCS using synchrotron radiation

Manfred Winnewisser, Brenda P. Winnewisser and Frank C. De Lucia
Department of Physics, The Ohio State University, Columbus Ohio, 43210-1106, USA

Dennis W. Tokaryk and Stephen C. Ross
Department of Physics and Centre for Laser, Atomic,
and Molecular Sciences, University of New Brunswick,
P.O. Box 4400, Fredericton, New Brunswick E3B 5A3, Canada

Brant E. Billinghurst
Canadian Light Source Inc., University of Saskatchewan,
44 Innovation Blvd, Saskatoon, Saskatchewan S7N 2V3, Canada
(Dated: March 27, 2014)

Quantum monodromy has a dramatic and defining impact on all those physical properties of chain-molecules that depend on a large-amplitude bending coordinate, including in particular the distribution of the ro-vibrational energy levels. As revealed by its pure rotational (a-type) spectrum [B.P. Winnewisser et al., Phys. Chem. Chem. Phys., 2010, 12, 8158-8189] cyanogen iso-thiocyanate, NCNCS, is a particularly illuminating exemplar of quantum monodromy. NCNCS, since it clearly shows the distinctive monodromy-induced dislocation of the ro-vibrational energy level pattern for its low-lying bending mode. This dislocation centers on a lattice defect in the energy vs. momentum map of the ro-vibrational levels at the top of the barrier to linearity, and represents an example of an excited state quantum phase transition [D. Larese and F. Iachello, J. Mol. Structure 1006, 611-628 (2011)]. To complete the data, so far limited to $\Delta J = +1$ transitions, we decided to measure the high-resolution far-infrared band of the large-amplitude bending vibration ν_7, and if possible also the along with mid-infrared bands. This Perspectives article presents our ongoing progress towards this goal, beginning with the description of how to predict line positions and intensities of the a- and b-type bands of the large amplitude bending mode using the Generalized-SemiRigid-Bender (GSRB) Hamiltonian for NCNCS and *ab initio* dipole moment functions [B.P. Winnewisser et al., Phys. Chem. Chem. Phys., 2010, 12, 8158-8189]. We include background information about synchrotron physics to clarify the advantages and limitations of that radiation source for our experiments. Details of the chemical preparation and sample handling, leading to the realization that NCNCS is 50 kJ/mol lower in energy than $S(CN)_2$ [Z. Kisiel et al., J. Phys. Chem. A, 2013, 117, 13815-13824] are included. We present the far-infrared and mid-infrared spectrum of NCNCS obtained at the Canadian Light Source synchrotron, using the IFS 125HR Bruker Fourier transform spectrometer. Eight of the fundamental vibrational modes of NCNCS have now been observed at high resolution. Initial analyses of the data confirm band assignments and demonstrate the accuracy of the predictions.

1. INTRODUCTION

In their Editorial to the *Themed issue: Chemical Dynamics of Large Amplitude Motion* published in Physical Chemistry and Chemical Physics [1] David J. Nesbitt and Martin A. Suhm expressed beautifully the problem inherent to the physical, chemical and mathematical aspects of large amplitude motion in molecular systems: *...This is the interesting and yet challenging world of large amplitude dynamics, where eigenfunctions do not factor cleanly into products, simple quantum mechanical solutions do not generally exist and the coupling between conventionally well isolated degrees of freedom (e.g. vibration/rotation) can become the dominant terms in the Hamiltonian...* In our contribution to that special issue [2] we demonstrated that the large amplitude ro-vibrational dynamics of the low-lying bending mode in NCNCS is intimately linked to the topology of the surfaces of constant energy in the four-dimensional phase space associated with motion constrained by the potential function. Monodromy resulting from the champagne-bottle bending potential is strongly imprinted on the wavefunctions and patterns of energy levels associated with this mode. Generalized-SemiRigid-Bender (GSRB) Hamiltonian calculations show that all important physical quantities, including effective rotational constants, ro-vibrational energies, and the expectation values of the electric dipole moment components, show the effects of quantum monodromy, providing an example of an excited state quantum phase transition [3, 4].

Reference [2] was based only on the pure (end-over-end) rotational spectrum of the molecule in the millimeter wave region. In the present work we have expanded this work into the Far-Infrared (FIR) and mid-infrared

(MIR) spectral regions. We present a detailed account of how the FIR transition line intensities can be calculated. The challenges of the experimental work necessary in our pursuit of the signatures of NCNCS quantum monodromy in the FIR and MIR spectral regions are discussed. Initial results are reported from the spectra obtained.

The remainder of the paper is organized as follows: Section 2 reviews the background of quantum monodromy associated with a champagne bottle potential function. The calculation of the far-infrared spectral line positions and their intensities for the large amplitude bending mode CNC ν_7 of NCNCS indicated in **Fig. 1** is presented in section 3. Subsection 3.1 provides the derivation of the electric dipole transition moments using the GSRB Hamiltonian wavefunctions. The remaining subsections of Section 3 show the resulting prediction of the a-type and b-type spectrum of NCNCS in the far-infrared region.

We feel that it is important to understand the decision to measure the complex FIR spectrum in high resolution at the Canadian Light Source. Section 4 therefore discusses the far infrared beamline and the generation of synchrotron light for the perspective of a chemist. Section 5 presents the chemical preparation of NCNCS, the unexpected challenges, and finally the high resolution spectroscopy, following three measuring campaigns in 2011, 2012, and 2013. The main conclusions and perspectives for 2014, our last measuring campaign, are summarized in section 6.

2. BACKGROUND

The concept of monodromy (Greek for "once around) for the dynamics of a particle in a potential energy function shaped like the bottom part of a champagne bottle was introduced by Larry Bates [5] in 1991. This potential energy function is circularly symmetric with two conserved physical quantities: energy and angular momentum. Bates pointed out that the surfaces of constant energy in phase space had distinct topologies as labelled in **Fig. 1**: $S^2 \times S^1$, a torus in this four-dimensional space, for energies below the top of the hump, and S^3, a topological sphere, in regions above. The topological change that occurs in crossing the critical energy point at the top of the hump indicates that the variables used to define the classical motion will necessarily be different in each region, so no global set of variables exists to describe the motion in all regions. This is a fundamental and robust property of such two-dimensional potential surfaces. In a quantum mechanical molecular system, classical monodromy translates into a dislocation or defect in the pattern of discrete energy levels in the energy-momentum map [6–11]. The change in topology involves the reclassification of one degree of freedom from rotational (below the barrier) to vibrational (above the barrier) [2, 11]. In their recent publication Larese and Iachello [3] applied the concept of Quantum Phase Transitions (QPT) to such systems and introduced the term "Excited State Quantum Phase Transition" (ESQPT) for molecules exhibiting large amplitude bending motion which show quantum monodromy in their energy-momentum maps.

Cyanogen iso-thiocyanate, NCNCS, is the best model system found so far for a molecule that clearly exhibits a distinctive monodromy-induced dislocation in the energy level pattern. The large-amplitude ν_7 bending mode of NCNCS (see **Fig. 1** and **Fig. 2**) can be studied from the ground state to levels above the barrier, with very little interference from other vibrational excitations [2, 10, 11, 13]. The connection between the bending motion of NCNCS and the champagne bottle potential function can be understood by considering the schematic potential shown on the left hand side of **Fig. 1**. There the radial coordinate can represent the ν_7 bending motion of the molecule with the origin (where the hump of the potential lies) corresponding to the linear configuration. For NCNCS the angular coordinate in this schematic figure then represents rotational motion around the long-axis (a-or z-axis) of the molecule. It is the nature of the coupling between these two motions that leads to monodromy in NCNCS. The bending potential energy function is obtained by any radial cut through the surface in **Fig. 1**. For NCNCS the actual bending potential energy function is shown below, in **Fig. 3**. We used the fast sub-millimeter spectroscopic technique (FASSST) [14–16] to extend the early microwave measurements [13] into the millimeter and sub-millimeter wave region [2, 10]. The analysis of 9204 pure rotational lines with rotational quantum numbers up $J \cong 100$ and assigned to 7 vibrational states of the CNC quasi-linear bending mode showed that the topological properties of the bending potential energy function are mapped onto the rotational and ro-vibrational energy levels as is shown in **Fig. 2**. Panel **a** shows the experimental (dots connected by lines) and calculated quantum lattice (dots) of effective rotational constants B_{eff} as a function of the angular momentum quantum number K_{a} and the vibrational quantum number v_{b} for the bent limiting case [2]. These B_{eff} values represent the end-over-end rotational contribution to the energy. The Generalized Semi-Rigid-Bender (GSRB) Hamiltonian [2] allowed us to calculate from this data the bending-rotation term values $[E(K_{\mathrm{a}}, v_{\mathrm{b}})]$/hc with an estimated uncertainty of approximately $\pm 1.5\,\mathrm{cm}^{-1}$ in the states $v_{\mathrm{b}} \leq 5$. In panel **b** of **Fig. 2** they are plotted for $J = K_{\mathrm{a}}$ versus K_{a} yielding a two-dimensional energy-momentum map. This bending energy-momentum map is the starting point of this paper.

We arranged to measure the far-infrared spectrum of both $S(CN)_2$ and NCNCS at high-resolution using the synchrotron radiation of the Canadian Light Source

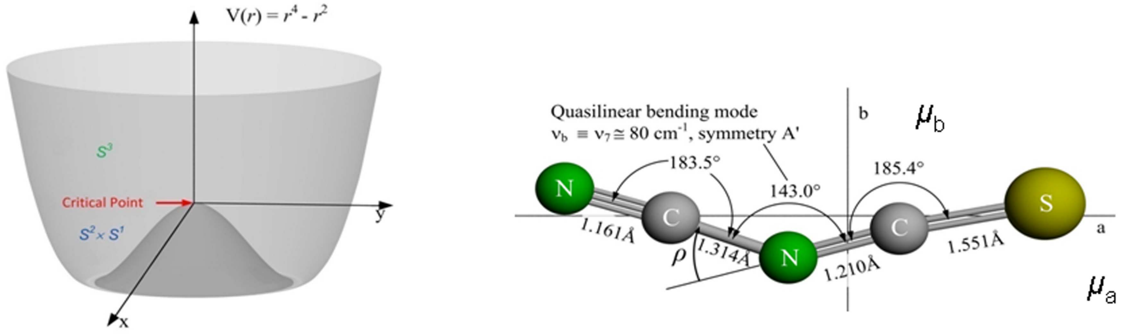

FIG. 1: The left-hand panel of this figure shows a schematic champagne bottle potential energy function for the quasi-linear in-plane bending mode of NCNCS. The large-amplitude coordinate ρ is defined on the molecular structure in the right-hand panel. The critical point of the potential function is indicated together with the topologies of phase-space surfaces of constant energy above and below this point [11]. The equilibrium structure of NCNCS from *ab initio* calculations with CCSD(T)/cc-pV5Z level of theory is given in the right-hand panel [10].

TABLE I: Low resolution IR wavenumbers and ab initio predicted harmonic and anharmonic fundamental vibrational modes for NCNCS (Symmetry C_s) including intensities.

	Γ	$\nu_{exp-gas}{}^a$ /cm^{-1}	ω^b /cm^{-1}	ν^b /cm^{-1}	MP2 Intensities^c in km/mol	Harmonic potential energy distribution **[N(1)C(2)N(3)C(4)S(5)]**
ν_1	A'	2260.5	2302	2258	924	73 % 1-2 s^d, 22% 2-3 s
ν_2	A'	2017.0	2058	2024	611	74 % 3-4 s, 15% 4-5 s, 10% 1-2 s
ν_3	A'	1185.0	1188	1178	10	47 % 2-3 s, 41% 4-5 s, 13% 1-2 s
ν_4	A'		688	662	2	39 % 4-5 s, 31% 2-3 s, 25% 3-4 s
ν_5	A'	481.0	483	472	28	68 % 3-4-5 b, 19% 1-2-3 b, 11% 2-3-4 b
ν_8	A''	445.0	452	454	4	65 % 2-3-4-5 t, 35% 1-2-3-4 t
ν_6	A'		444	447	13	74 % 1-2-3 b, 25% 3-4-5 b
ν_9	A''		430	429	5	65 % 1-2-3-4 t, 35% 2-3-4-5 t
ν_7	A'		**89**	**80**	**4**	**94% 2-3-4 in-plane large amplitude bend**

[a] Low resolution gas phase wavenumbers and intensities were reported in 2007 by Wang [12].

[b] ω stands for harmonic wavenumber in cm^{-1}, ν for anharmonic wavenumber in cm^{-1}, see Ref. [10].

[c] Private communication by Jacek Koput.

[d] s stands for stretching, b for bending, t for torsional vibration.

(CLS) in Saskatoon, Saskatchewan, Canada. NCNCS is most efficiently synthesized by pyrolysis of its $S(CN)_2$ isomer, so it was essential to determine the $S(CN)_2$ spectrum, in order to sort out its lines from those of NCNCS. Furthermore, $S(CN)_2$ [18, 19], provides the spectrum of a rather rigid bent molecule, in stark contrast to NCNCS. In this paper we report what we consider to be important aspects of the project, outlining a series of challenges which had to be overcome in the realm of chemical sample preparation and handling, theoretical spectroscopy in predicting the NCNCS far-infrared absorptions and their intensities, and the actual high-resolution measurements at the Far-Infrared Beamline of the CLS.

3. THE PREDICTION OF THE FAR-INFRARED SPECTRAL LINE POSITIONS AND THEIR INTENSITIES FOR NCNCS

Table I gives the *ab initio* predicted harmonic and anharmonic fundamental vibrational modes for NCNCS with symmetry C_s [2, 10, 12]. The two strongest stretching vibrational modes are ν_1 and ν_2 of NCNCS. The large amplitude CNC bending mode ν_7 is among the three weakest of the infrared absorptions, and its spectrum is located at 80 cm^{-1}, which is experimentally a rather difficult spectroscopic region. In addition we learn that the CNC bending mode ν_7 of NCNCS with its term value of 80 cm^{-1} is almost completely isolated from all the other bending and stretching vibrational modes. We can

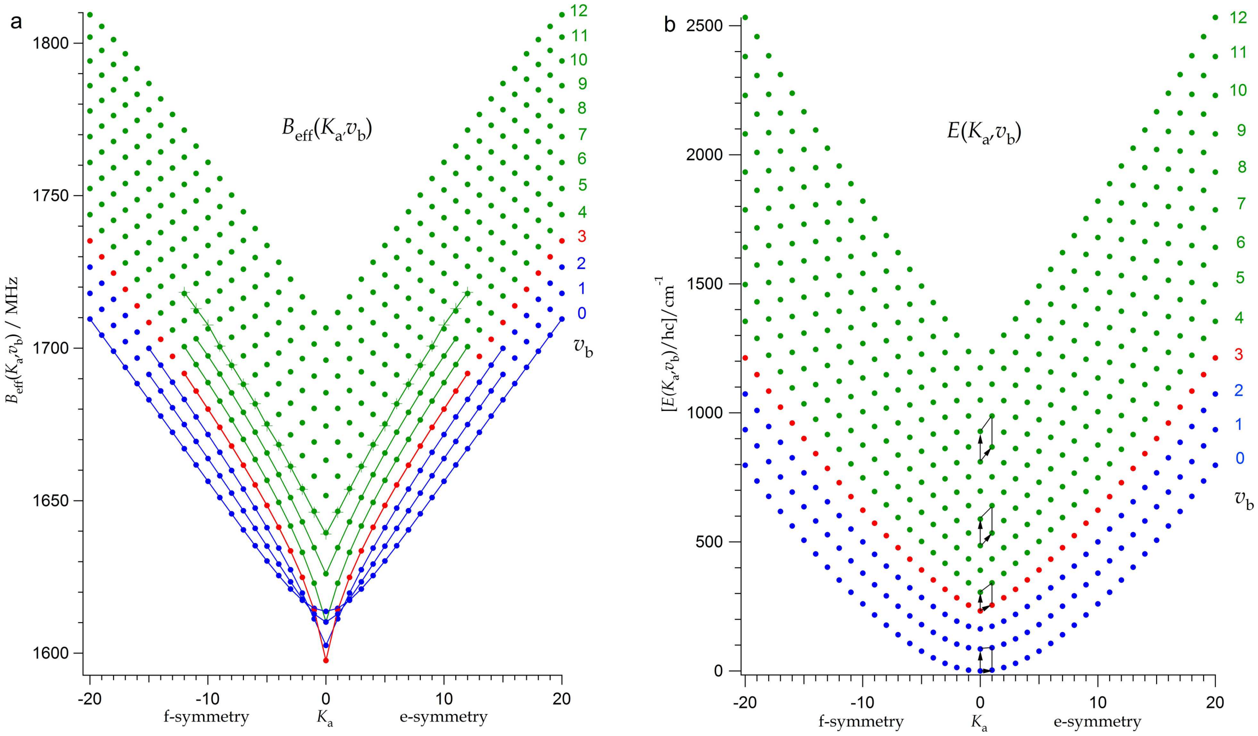

FIG. 2: Monodromy plots for NCNCS were taken from Ref. [2]. Panel **a** shows the experimental and calculated quantum lattice of the effective rotational constants B_{eff} as a function of K_{a} and v_{b}, representing the end-over-end rotational energy contribution. The experimental B_{eff} values are connected by lines while the theoretical GSRB predictions are not. The experimental data for $v_{\mathrm{b}} = 6$, which are shown as small crosses, were not included in the fitting. They are almost indistinguishable from the GSRB predictions. Panel **b** shows the corresponding GSRB calculated two-dimensional energy-momentum map for NCNCS represented by the bending-rotation term values $[E(K_{\mathrm{a}}, v_{\mathrm{b}})]/\mathrm{hc}$ for $J = K_{\mathrm{a}}$. The data due to asymmetry splitting for the lower K_{a} values were averaged, and the plots extended to $K_{\mathrm{a}} < 0$ (by reflection in the vertical plane) to be analogous to the classical case. The following color scheme was adopted: Blue entries in both panels arise from energy levels whose $K_{\mathrm{a}} = 0$ level is below the monodromy point; for red entries the $K_{\mathrm{a}} = 0$ level is located near the monodromy point while for green entries the $K_{\mathrm{a}} = 0$ levels are above the monodromy point. If one follows the unit cell indicated in the energy-momentum map (panel **b**) from the blue region to the green region one clearly notices the distortion which is indicative of the transition from a bent molecular structure to a linear one [2, 11, 17]. The data due to asymmetry splitting for the lower K_{a} values were averaged, and the plots extended to $K_{\mathrm{a}} < 0$ to be analogous to the the classical case. The e- and f-symmetry designation is independent of J.

deduce from the geometry of NCNCS that this in-plane bending transition moment will have components along both the a and b principal axes of inertia. (The a-axis is the principal axis with the smallest moment of inertia, the c-axis is that with the largest moment of inertia, and the b-axis is the intermediate case). We therefore expect to observe a hybrid band system consisting of both a- and b-type transitions. What is the situation now for the quasi-linear molecule NCNCS, in which a rotational degree of freedom in the bent limiting case becomes a vibrational degree of freedom [11] when the molecule is excited to states above the potential hump? If we follow the unit cells in the energy-momentum lattice, indicated in **Fig. 2** panel **b**, from the bottom to the top, we observe a strong deformation of the unit cells which is indicative of an excited state quantum phase transition (see Ref. [2] Fig. 18 and Ref. [3, 4]). This transition raises a variety of questions: What will the ro-vibrational spectrum of the bending fundamental look like? Do we observe b-type or a hybrid band system? How will the intensities evolve upon excitation? Can observation of the appropriate far-infrared band systems allow us to build up a fully experimental version of the ro-vibrational energy momentum lattice to match the GSRB predicted one of **Fig. 2** panel **b**?

In Ref. [2] we presented a detailed derivation of the Generalized Semi-Rigid Bender Hamiltonian (GSRB) which was successfully applied to the NCNCS problem. The Hamiltonian operator was partitioned into two parts. The first part is a large-amplitude vibrational part which corresponds to the CNC bending mode plus a z-axis (or a-axis) rotational part. The second part is the end-over-end rotational motion of the molecule, including the terms involving rotation about the x or y-axes,

$$\hat{H}_{\mathrm{SRB}} = \hat{H}_{\mathrm{LAvib}+z-\mathrm{rotation}} + \hat{H}_{x-y-\mathrm{rotation}}. \qquad (1)$$

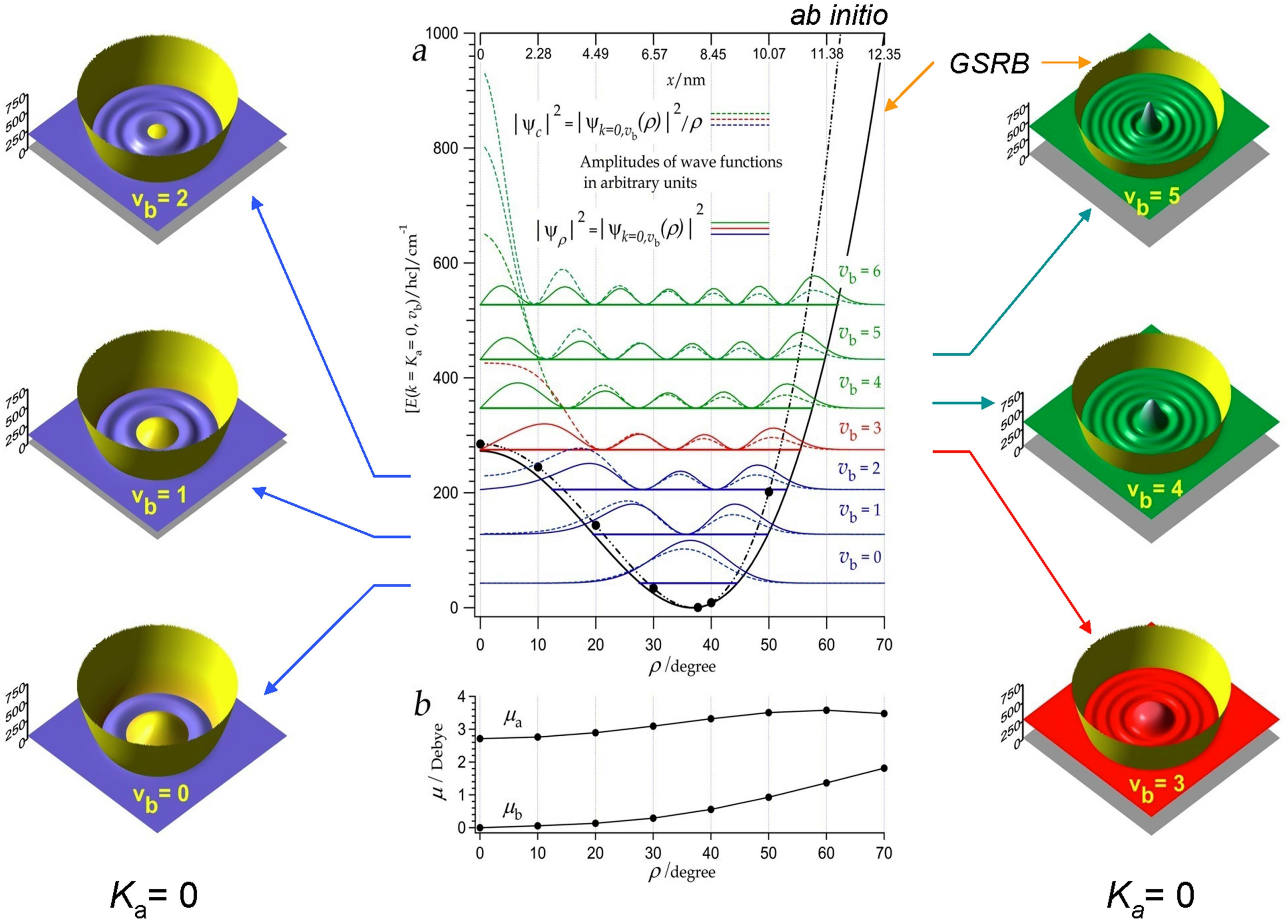

FIG. 3: The central panel with parts **a** and **b** of this figure is taken from our recent PCCP paper [2]. The solid black line represents the dependence of the potential energy on the bending coordinate ρ, obtained by fitting the Generalized Semi-Rigid Bender Hamiltonian (GSRB) to our experimental data. The solid black dots are the calculated *ab-initio* values. The probability densities $|\Psi_\rho|^2$ and $|\Psi_c|^2$ for v_b and $K_a = 0$ are given for both polar and Cartesian coordinates for all observed values of v_b. We plot $|\Psi_c|^2$ in cartoons for each wave function indicated in the central panel, and obtain a feeling for the stationary state probability density in the Cartesian representation. The champagne bottle potential is plotted in golden color. We clearly see that $|\Psi_c|^2$ has a maximum at the origin (i.e. linearity) as soon as we have reached the classical monodromy point which lies slightly below the energy of the $v_b = 3$, $K_a = 0$ vibrational state. Part **b** of the central panel depicts the dependence on ρ of the *ab initio* calculated electric dipole moment components μ_a and μ_b.

The solution of the Schrödinger equation for this Hamiltonian is carried out in two steps. The large-amplitude + z-rotation basis set is obtained by solving its Schrödinger equation,

$$\hat{H}_{\text{LAvib}+z-\text{rotation}}\Psi_{k,v}(\rho,\chi) = E_{k,v}\Psi_{k,v}(\rho,\chi) \quad (2)$$

for the product wave function,

$$\Psi_{k,v}(\rho,\chi) = \frac{1}{\sqrt{2\pi}}e^{ik\chi}\psi_{k,v}(\rho), \quad (3)$$

where k is the quantum number associated with rotation about the z-axis while v corresponds to the large-amplitude bending quantum number. (Note: This corresponds to the definition of v for a bent asymmetric rotor molecule, or the radial quantum number n when using polar coordinates for a linear molecule.) The Euler angle χ describes the rotation about the a- (or z-) axis with the smallest moment of inertia. ρ is the large amplitude bending coordinate defined in **Fig. 1** which displays the equilibrium structure of NCNCS in the principal axes system.

In the second step the product basis functions $\Psi_{k,v}(\rho,\chi)$ of **eqn (3)** are multiplied by "end-over-end" rotational factors, that is by the θ,φ parts, $S_{Jkm}(\theta,\varphi)$, of the normalized symmetric rotor wave functions. This gives the full Semi-Rigid Bender (SRB) basis functions of Eq. 14 of Bunker and Stone [20],

$$\begin{aligned}\Psi_{J,k,m,v}(\theta,\varphi,\chi,\rho) &= S_{j,k,m,}(\theta,\varphi)\Psi_{k,v}(\rho,\chi)\\ &= |Jkm\rangle\psi_{k,v}(\rho),\end{aligned} \quad (4)$$

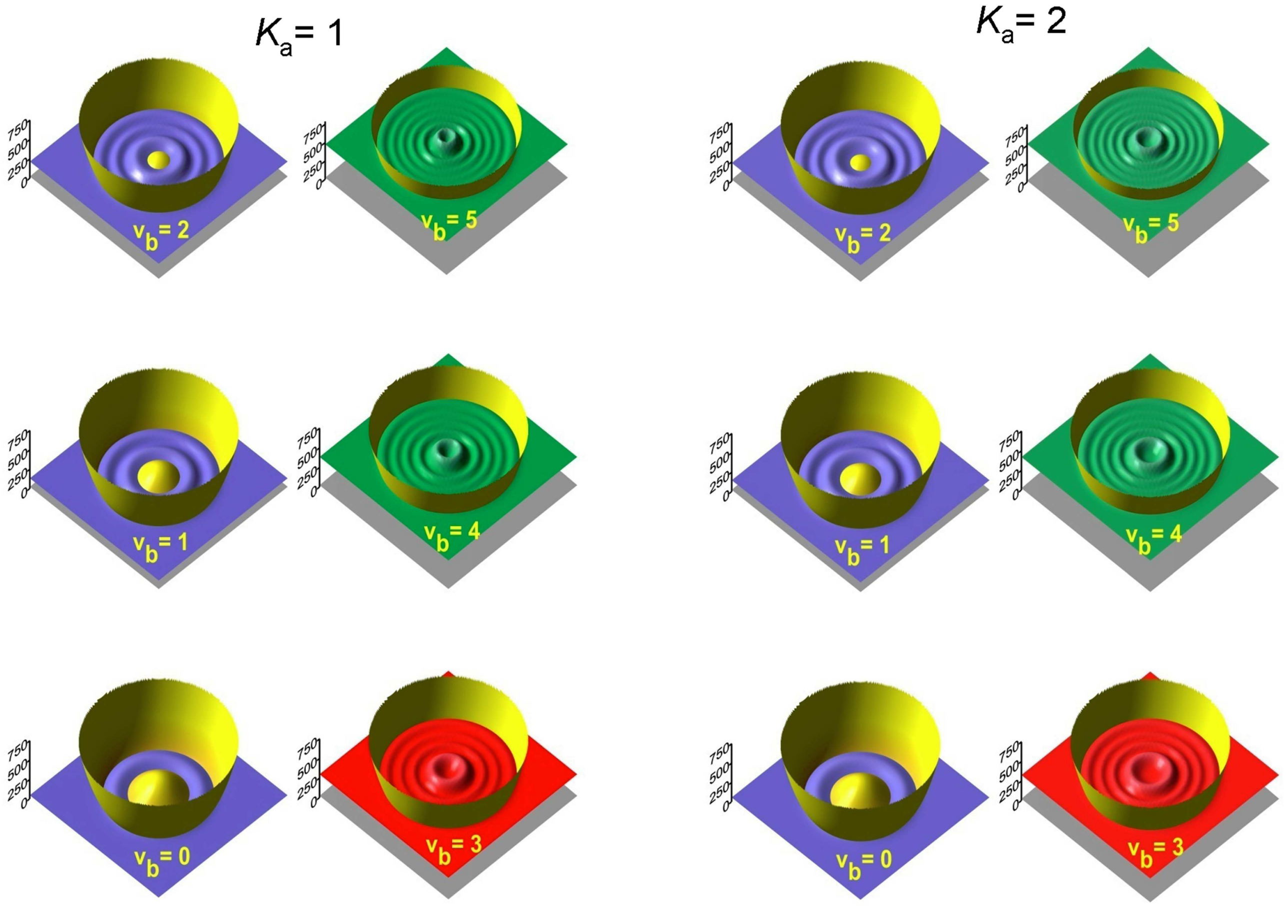

FIG. 4: An extension of **Fig. 3** to the angular momentum quantum numbers $K_{\mathrm{a}} = 1$ and $K_{\mathrm{a}} = 2$. Above the monodromy point the probability density of the wave function squared $|\Psi_{\mathrm{c}}|^2$ is no longer a maximum at $x = 0$. The probability density that the molecule will be bent to a particular value of ρ can be seen for each v_{b} values both above and below the monodromy point as a probability density ring around the origin.

where $|Jkm\rangle$ are normalized symmetric top wave functions and where the $\psi_{k,v}(\rho)$ are independent of the sign of k since Eq. 29 in Ref. [2] depends on k^2. The GSRB Hamiltonian for all 4 degrees of freedom was then diagonalized in this basis yielding wavefunctions and level energies.

The GSRB fitted potential energy function for the large amplitude bending motion is shown in the center of **Fig. 3**. Also shown, by the round dots are the *ab initio* potential energy values. The GSRB potential energy function includes the variation with ρ of the zero-point energy of all the small-amplitude vibrations and is not expected to be identical to the *ab initio* function.

Probability densities (PDs) are given by the square moduli of the wavefunctions. **Fig. 3** and **Fig. 4** show PDs for the basis functions of **eqn (3)** with $K_{\mathrm{a}} = 0$ and $K_{\mathrm{a}} = 1, 2$, respectively. These are plotted in polar form with the bending coordinate, ρ, used as the radial coordinate and the axial rotational coordinate, χ, used as the angular coordinate. The GSRB program first calculates the $\psi_{k,v}(\rho)$ functions. **Eqn (3)** immediately implies $|\Psi_{k,v}(\rho,\chi)|^2 = \frac{1}{2\pi}|\psi_{k,v}(\rho)|^2$ which corresponds to the probability density of the molecule having a particular bent configuration, ρ, but a completely unspecified orientation, χ.

In the polar representation this corresponds to the probability of the molecular configuration-orientation lying in a ring of radius ρ and width $d\rho$. Another way of saying this is that the $\psi_{k,v}(\rho)$ functions are defined relative to a volume element $d\rho$, rather than the $\rho\, d\rho$ volume we are accustomed to. Therefore, to plot the PDs in the full two-dimensional polar form we must realize that for a given value of ρ the probability density $|\psi_{k,v}(\rho)|^2$ is distributed over the entire ring from $\chi = 0$ to $\chi = 2\pi$, that is, over a ring of circumference $2\pi\rho$. The factor of $\frac{1}{2\pi}$ is already accounted for by the relationship between $\Psi_{k,v}(\rho,\chi)$ and $\psi_{k,v}(\rho)$.

However, to plot the PD in full two-dimensional form we must still divide $|\Psi_{k,v}(\rho,\chi)|^2$ by ρ, to have a form corresponding to the usual volume element $\rho\, d\rho$. We re-

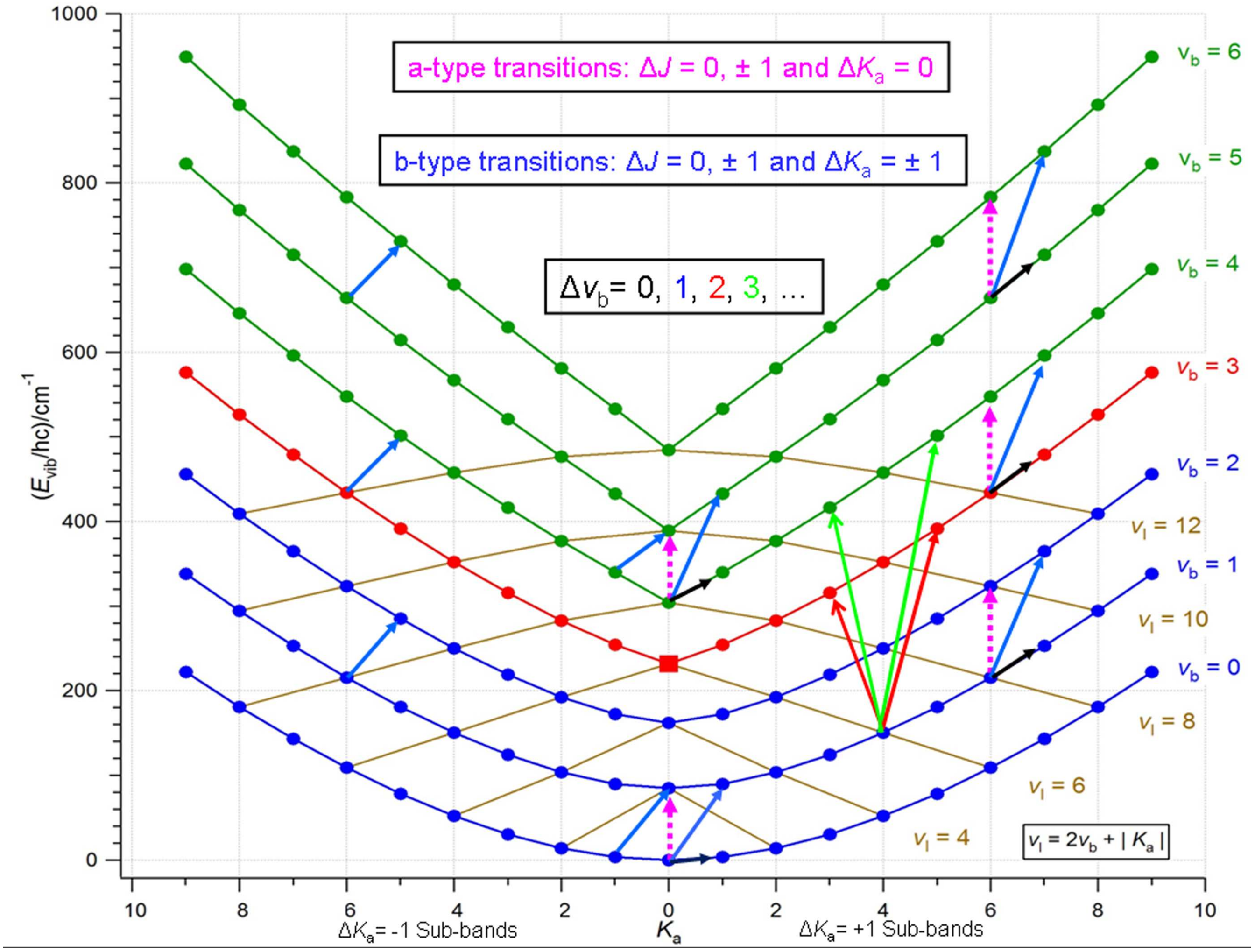

FIG. 5: An excerpt of the energy-momentum plot for NCNCS given in **Fig. 2**. We label the vibrational level series with v_{b} using the bent notation and also with v_{l}, the notation of a linear molecule ($v_{\mathrm{l}} = v_{\mathrm{linear}}$). They are related by $v_1 = 2v_{\mathrm{b}} + |K_{\mathrm{a}}|$. The ro-vibrational energies of the levels $J = K_{\mathrm{a}}$ are plotted as a function of K_{a}, which is approximately a good quantum number. However, neither v_{b} nor v_{l} are good quantum numbers in all regions of the map due to monodromy in the champaign bottle potential. The energy level which is closest to the monodromy point of the potential energy function is indicated by a red square in the middle of the graph labeled with $v_{\mathrm{b}} = 3$. Examples are shown of transitions that follow the usual selection rules for a-type (in dotted purple) and b-type (in solid black and blue). Transitions with $\Delta v_{\mathrm{b}} = 2\,\mathrm{or}\,3$ predicted to have significant intensity are shown by longer red and green arrows. The ro-vibrational term values series originating below the monodromy point are in blue, at the monodromy point in red, and above in green.

fer to these converted PDs as Cartesian PDs, $|\Psi_{\mathrm{c}}| = |\Psi_{k,v}(\rho,\chi)|^2/\rho$ ("c' for Cartesian), and these are what are plotted in **Fig. 3** and **Fig. 4**. An important point related to this is that the form of the singularity of the extended moment of inertia matrix at linearity means that the $\psi_{k,v}(\rho)$ functions appearing in **eqn (3)** are of the form $\psi_{k,v}(\rho \to 0) \approx \rho^{\frac{1}{2}+|k|}$ and therefore all go to zero as ρ goes to zero. For the Cartesian form of the PDs, that is after dividing by ρ, this means that the PDs must go to zero as ρ goes to zero if $K_{\mathrm{a}} \to 0$, but not if $K_{\mathrm{a}} = 0$. This can be easily seen by comparing the PDs in **Fig. 3** ($K_{\mathrm{a}} = 0$) and **Fig. 4** ($K_{\mathrm{a}} = 1, 2$), especially for energies above the monodromy point.

As pointed out in section 5.4 of Ref. [2] the effects of monodromy are also mapped into the expectation values of the bending coordinates ρ and ρ^2, the electric dipole moment components μ_{a} and μ_{b} and the effective rotational constants B_{eff}. It is therefore predictable that the wave functions given in **eqn (3)** that carry this monodromy information will also strongly affect the transition intensities for NCNCS.

3.1 The derivation of the electric dipole transition moments determining the FIR transition intensities for NCNCS

The large-amplitude of the ν_7 (CNC bending) vibration means that the inverse moments of inertia of the molecule cannot be treated as constants during this motion which is why the ν_7 vibrational mode cannot be separated from the rotational motion [2]. It is because of this that we have used the GSRB to model the ν_7 bending + rotational energy levels of NCNCS. For the same reason we use the GSRB to calculate the transition intensities for NCNCS.

The theoretical calculation of the intensities of electric dipole-induced transitions begins with the fact that the energy due to the interaction between an external electric field vector and an electric dipole moment vector is $-\vec{\mu}\cdot\vec{E}$. For a sinusoidally oscillating external electric field with angular frequency ω, $\vec{E}(t) = \vec{E}_0 e^{i\omega t}$, the calculation of the population transfer rate (Variable: *Rate*) for a transition from a state Ψ_i to a state Ψ_f can be done using first order time-dependent perturbation theory. This results in Fermi's golden rule (which was actually first derived by Dirac [21]),

$$Rate_{f\leftarrow i}(\omega) = \frac{2\pi}{\hbar^2}|\langle\Psi_f \mid -\vec{\mu}\cdot\vec{E}_0|\Psi_i\rangle|^2\delta(\omega_{fi}-\omega). \quad (5)$$

Here $\omega_{fi} = (E_f - E_i)/\hbar$ where E_f and E_i are the energy levels of the atomic or molecular species and it is assumed that the wavelength of the oscillating electric field is much larger than the size of the molecular system under consideration. When ω is integrated over the transition frequency, ω_{fi}, the Dirac delta function gives a unit value. It is that integrated result that is of use in considering transition probabilities when the incident wave is resonant with the transition frequency. Two factors usually complicate the evaluation of the matrix element in **eqn (5)**. First, the wave functions for the initial and final states are often linear combinations of a set of basis functions. For NCNCS the basis functions for a given J and m are given in **eqn (4)**. Ψ_i can thus be written as

$$\Psi_i = \sum_{k,v} a^i_{k,v}\Psi_{J,k,m,v} = \sum_{k,v} a^i_{k,v}|Jkm\rangle\Psi_{k,v}(\rho). \quad (6)$$

Similarly the wave function of the final state, Ψ_f, can be expanded as,

$$\Psi_f = \sum_{k',v'} a^f_{k',v'}\Psi_{J',k',m',v'} = \sum_{k',v'} a^f_{k',v'}|J'k'm'\rangle\psi_{k',v'}(\rho). \quad (7)$$

Since the SRB Hamiltonian of **eqn (1)** does not mix different values of either the total angular momentum, J, or of its spaced fixed projection, m, both Ψ_i and Ψ_f have well defined J and m values, which we denote as J, m and J', M', respectively. (In principle these indices should be added to the notation for Ψ_i and Ψ_f and to the $a^i_{k,v}$ and $a^f_{k',v'}$ expansion coefficients but for clarity we do not do so). Therefore the summations in **eqn (6)** and **eqn (7)** do not include either J or m. The $a^i_{k,v}$ and $a^f_{k',v'}$ expansion coefficients are those obtained by the diagonalisation of the SRB Hamiltonian. The ranges of summation of k and of k' obviously depend on the values of J and J', respectively. The evaluation of the factor inside the square modulus of **eqn (5)** therefore requires a double sum over basis set elements, one sum for the basis for J, m corresponding to Ψ_i, the other for the basis for J', m' corresponding to Ψ_f. Furthermore, in the case of NCNCS, the dipole moment is not constant but instead varies with the bending angle ρ, so that $\vec{\mu} = \vec{\mu}(\rho)$. The matrix element in **eqn (5)** thus becomes,

$$\begin{aligned}
&\langle\Psi_f|\vec{E}_0\cdot\vec{\mu}(\rho)|\Psi_i\rangle = \vec{E}_0\cdot\langle\Psi_f|\vec{\mu}(\rho)|\Psi_i\rangle \\
&= \vec{E}_0\cdot\sum_{k',v'}(a^f_{k',v'})^*\langle J'k'm'|\langle\psi_{k',v'}(\rho)|\vec{\mu}(\rho) \\
&\qquad \sum_{k,v} a^i_{k,v}|Jkm\rangle|\psi_{k,v}(\rho)\rangle \qquad (8)\\
&= \vec{E}_0\cdot\sum_{k',v'}\sum_{k,v}(a^f_{k',v'})^* a^i_{k,v}\langle J'k'm'|\langle\psi_{k',v'}(\rho)|\vec{\mu}(\rho) \\
&\qquad |\psi_{k,v}(\rho)\rangle|Jkm\rangle.
\end{aligned}$$

(Since the rotational functions $|Jkm\rangle$ do not depend on ρ and the vibrational functions $\psi_{k,v}(\rho)$ do not depend on the Euler angles these two kets can be written in either order, as can the associated bras.)

The second complicating factor in evaluating transition probabilities in molecules is that while the external electric field vector amplitude, $\vec{E}_0$, is defined relative to axes parallel to the laboratory frame (lab fr), $\ell = X, Y, Z$, the dipole moment components of the molecule, $\vec{\mu}(\rho)$, are defined relative to the molecule-fixed axis, (mol fr) $j = x, y, z$. As in Ref. [2] we denote by **C** the direction cosine matrix for transformation from space-fixed to molecule-fixed axis. **C** is the equivalent of the λ matrix of Eqn (10-5) to Eqn (10-7) of Bunker and Jensen [22].

$\mathbf{C}^t$ is then the transformation matrix in the opposite sense. We can therefore write the components of the molecular dipole moment relative to the laboratory frame (lab fr) in terms of components relative to the molecular frame (mol fr) as,

$$\mu^{\text{lab fr}}_{\ell}(\rho) = \sum_{j=x,y,z}\mathbf{C}^t_{\ell,j}\mu^{\text{mol fr}}_j(\rho), \quad (9)$$

for $\ell = X, Y, Z$.

Denoting the unit vectors $\hat{X}, \hat{Y}, \hat{Z}$ parallel to the laboratory frame (*lab fr*) as $\hat{X}_\ell$, where $\ell = 1, 2, 3$, the molecular dipole moment vector can then be written in terms of the molecule-fixed components as

$$\begin{aligned}\vec{\mu}(\rho) &= \sum_{\ell=X,Y,Z} \mu_\ell^{\mathrm{lab\,fr}}(\rho)\hat{X}_\ell \\ &= \sum_{\ell=X,Y,Z}\sum_{j=x,y,z} \mathbf{C}^t_{\ell,j}\mu_j^{\mathrm{mol\,fr}}(\rho)\hat{X}_\ell,\end{aligned} \tag{10}$$

and similarly the vector amplitude, $\vec{E}_0$, of the external electric field can be written as,

$$\vec{E}_0 = \sum_{\ell=X,Y,Z} E_{0,\ell}\hat{X}_\ell. \tag{11}$$

Substituting **eqns (9)** through **(11)** into **eqn (8)**, using the orthonormality of the $\hat{X}_\ell$ unit vectors, and noting that the direction cosine elements $\mathbf{C^t}$ depend solely on rotational coordinates and not on ρ, we obtain,

$$\begin{aligned}&\langle\Psi_f|\vec{E}_0\cdot\vec{\mu}(\rho)|\Psi_i\rangle \\ &= \vec{E}_0\cdot\sum_{k',v'}\sum_{k,v}(a^f_{k',v'})^* a^i_{k,v}\langle J'k'm'|\langle\psi_{k',v'}(\rho)|\vec{\mu}(\rho) \\ &\qquad |\psi_{k,v}(\rho)\rangle|Jkm\rangle \\ &= \sum_{\ell=X,Y,Z} E_{0\ell}\sum_{k',v'}\sum_{k,v}(a^f_{k',v'})^* a^i_{k,v}\langle J'k'm'|\langle\psi_{k',v'}(\rho)| \\ &\qquad \mu_\ell^{\mathrm{lab\,fr}}(\rho)|\psi_{k,v}(\rho)\rangle|Jkm\rangle \\ &= \sum_{\ell=X,Y,Z} E_{0\ell}\sum_{k',v'}\sum_{k,v}(a^f_{k',v'})^* a^i_{k,v}\langle J'k'm'|\langle\psi_{k',v'}(\rho)| \\ &\qquad \sum_{j=x,y,z}\mathbf{C}^t_{\ell j}\mu_j^{\mathrm{mol\,fr}}(\rho)|\psi_{k,v}(\rho)\rangle|Jkm\rangle \\ &= \sum_{\ell=X,Y,Z} E_{0\ell}\sum_{k',v'}\sum_{k,v}(a^f_{k',v'})^* a^i_{k,v} \\ &\qquad \sum_{j=x,y,z}\langle J'k'm'|\mathbf{C}^t_{\ell,j}|Jkm\rangle\langle\psi_{v',k'}(\rho)|\mu_j^{\mathrm{mol\,fr}}(\rho)|\psi_{k,v}(\rho)\rangle.\end{aligned} \tag{12}$$

Since the relative orientation of the rotating molecule and the lab frame is random we only need to calculate the probability for a transition for one orientation of the electric field, i.e. for one value of ℓ in **eqn (12)**. If, as is the case here, the molecules are not spatially aligned then the full probability for a transition is obtained by simply multiplying the result for one direction by three to account for the three independent spatial directions. This is accounted for below. Furthermore, we are interested in the transition strength intrinsic to the molecule and therefore do not include the electric field amplitude. We therefore only need to consider the matrix element for one value of ℓ,

$$\begin{aligned}&\langle\Psi_f|\mu_\ell^{\mathrm{lab\,fr}}(\rho)|\Psi_i\rangle \\ &= \sum_{k',v'}\sum_{k,v}(a^f_{k',v'})^* a^i_{k,v}\sum_{j=x,y,z}\langle J'k'm'|\mathbf{C}^t_{\ell,j}|Jkm\rangle \\ &\qquad \langle\psi_{k',v'}(\rho)|\mu_j^{\mathrm{mol\,fr}}(\rho)|\psi_{k,v}(\rho)\rangle.\end{aligned} \tag{13}$$

The square modulus of **eqn (13)** is then supplemented by additional factors to account for the number of molecules per unit volume, the population of the initial state, etc. In **eqn (13)** we have arrived at an expression that can be evaluated using the GSRB wave functions and ab initio electric dipole moment functions. The ρ dependent molecular frame components of the molecular dipole moment, $\mu_j^{\mathrm{mol\,fr}}(\rho)$, are available from the ab initio calculations reported in our previous work [2]. Since those ab initio components of the electric dipole moment were relative to principal axes they are rotated to the HBJ x, y, z axes system before the large set of required matrix elements,

$$\langle\psi_{k',v'}(\rho)|\mu_j^{\mathrm{mol\,fr}}(\rho)|\psi_{k,v}(\rho)\rangle, \tag{14}$$

is calculated. These matrix elements are calculated using Simpsons Rule Integration with the basis functions obtained in Step 1 of Section 2.2 of Ref. [2]. The resulting matrix elements must then be combined with the standard rotational matrix elements of the direction cosines,

$$\langle J'k'm'|\mathbf{C}^t_{\ell,j}|Jkm\rangle. \tag{15}$$

These factors were evaluated following Section D of the particularly useful article by di Lauro and Mills [23] where they outline the evaluation of the sum of rotation-vibration factors in the middle of **eqn (13)**. The first step is to rearrange that sum in the form,

$$\begin{aligned}&\sum_{j=x,y,z}\langle J'k'm'|\mathbf{C}^t_{\ell,j}|Jkm\rangle\langle\psi_{k',v'}(\rho)|\mu_j{}^{\mathrm{mol\,fr}}(\rho)|\psi_{k,v}(\rho)\rangle \\ &\quad = \langle Rot'|\mathbf{C}^t_{\ell,z}|Rot\rangle\langle vib'|\mu_z(\rho)|vib\rangle \\ &\qquad + \langle Rot'|\frac{1}{\sqrt{2}}(\mathbf{C}^t_{\ell,x}+i\mathbf{C}^t_{\ell,y})|Rot\rangle \\ &\qquad\quad \langle vib'|\frac{1}{\sqrt{2}}[\mu_x(\rho)-i\mu_y(\rho)]|vib\rangle \\ &\qquad + \langle Rot'|\frac{1}{\sqrt{2}}(\mathbf{C}^t_{\ell,x}-i\mathbf{C}^t_{\ell,y})|Rot\rangle \\ &\qquad\quad \langle vib'|\frac{1}{\sqrt{2}}[\mu_x(\rho)+i\mu_y(\rho)]|vib\rangle,\end{aligned} \tag{16}$$

where, for clarity, we have used obvious short-hands for the vibrational and rotational factors. Transitions resulting from the component of the molecule electric dipole moment parallel to the long-axis of a chain molecule (the a-axis which we have denoted the z-axis) are said to be parallel or a-type transitions. These are governed by the first term in the right-hand side of **eqn (16)**. Transitions arising from the remaining two terms of **eqn (16)** are due to components of the electric dipole moment perpendicular to the long-axis of the molecule and are therefore called perpendicular transitions. In the present case the molecule remains planar and the out-of-plane c component of the electric dipole moment is zero. Parallel and perpendicular transitions have distinct features. Both cases allow $\Delta J = 0, \pm 1$, while $\Delta K_\mathrm{a} = 0$ for parallel (a-type) transitions and $\Delta K_\mathrm{a} = \pm 1$ for perpendicular (b-type) transitions.

The vibrational matrix elements appearing here are trivially obtained from those already calculated in **eqn (14)**. Di Lauro and Mills express the rotational matrix elements appearing in **eqn (16)** as products of two "reduced matrix elements", one related to the space-fixed axes, the other to the molecule-fixed axes. The first of these is common to all terms appearing in **eqn (13)** and due to **eqn (5)** its square modulus will show up squared in the final result. Therefore di Lauro and Mills give a closed form expression for the space-fixed term, taking the square modulus, summing over the m degeneracies of the initial and final states, and multiplying by 3 to account for the three independent spatial directions mentioned above. The resulting values are given in the second column of their Table II [23]. The last two columns of that table give closed form expressions for the molecule-fixed axes components for the rotational factors in **eqn (16)**. It is important to note that the various factors of $1/\sqrt{2}$ in **eqn (16)** [their eqn (26)] are not reflected in their Table II and must be accounted for separately. The results of **eqn (16)** for each set of k', m', k, m can then be substituted into **eqn (13)** where they are supplemented by the wave function expansion coefficients and the result summed to obtain the matrix elements, $\langle \Psi_f | \mu_\ell^{\mathrm{lab\,fr}} | \Psi_i \rangle$. With this result the following quantity, proportional to the absorption transition intensity, is easily calculated,

$$\begin{aligned} T_{f,i}^{\mathrm{relative}} = \; & \tilde{\nu}_{f,i} e^{-\frac{E_i}{kT}} [1 - e^{-\frac{1}{kT}(E_f - E_i)}] \\ & 3 |\langle \Psi_f | \mu_\ell^{\mathrm{lab\,fr}} | \Psi i \rangle|^2, \end{aligned} \tag{17}$$

where $\tilde{\nu}_{f,i} = \omega_{f,i}/2\pi c = (E_f - E_i)/hc$ is the transition wavenumber or line position (this physical quantity can also be expressed in frequency units), and in the actual calculation the overall factor of 3 is already accounted for in Table II of di Lauro and Mills [23].

It is these values that are plotted in the stick-spectra of the top of **Fig. 6** and in **Figs. 7 - 11**. The actual absorption intensity could be determined from $T_{f,i}^{\mathrm{relative}}$ by accounting for the molecular number density and the level population density yielding,

$$S_{f,i}^{\mathrm{relative}} = \frac{8\pi^3}{3hc} L C g_i \frac{273.15\,\mathrm{K}}{T} \frac{1}{Q(T)} T_{f,i}^{\mathrm{relative}}, \tag{18}$$

where h is Planck's constant, c is the speed of light, L is the Loschmidt's number, C is the isotopic abundance, g_i is the degeneracy of energy level i, (not including the m-degeneracy which is already included in the matrix element), T is the absolute temperature, and $Q(T)$ is the partition function. Here the inherent coupling of the rotational motion in NCNCS with the large-amplitude bending motion means that we can not approximate $Q(T)$ in the usual form as a product of rotational and vibrational factors. However, a reasonable approximation would be to produce $Q(T)$ as a product of a *large amplitude vibration + rotational* factor and a *small amplitude vibrational* factor,

$$Q(T) \approx [Q_{\mathrm{LAvib+rotation}}(T)] \times [Q_{\mathrm{SAvib}}(T)]. \tag{19}$$

$Q_{\mathrm{LAvib+rotation}}$ could be calculated from energies obtained from the present GSRB calculation while Q_{SAvib} could be calculated using the vibrational fundamentals given in **Table 1**. This step will be the subject of a future communication when the high resolution FIR and IR spectra will be analyzed.

Most quantum states plotted in the energy-momentum map given in **Fig. 5** are, of course, degenerate in K_a except for $K_\mathrm{a} = 1$ and 2. Most higher K_a states are twofold degenerate. $K_\mathrm{a} = 3$ is probably observably split at high J; some levels are split by resonances.

The transitions calculated as described in this section are shown as stick-spectra in **Figs. 6 - 11**. To enhance the clarity of these figures they are limited to showing $J \le 10$ or $J \le 20$ and $v_\mathrm{b} \le 6$, rather than showing each sub-band over the experimentally observed range, that is up to J over 100. We first discuss the a-type transitions (Section 3.2), then the b-type transitions (Section 3.3).

3.2 The a-type spectrum of NCNCS in the Far-Infrared region

To make the complex structure of the total spectrum more easily perceived we limit the stick spectra for the calculated a-type spectra to $J \le 10$ and $v_\mathrm{b} \le 10$. This is illustrated in **Fig. 6** where we show the superposition of all the predicted a-type parallel sub-bands. The intensities given in arbitrary numbers in **Fig. 6** represent relative values of $T_{f,i}^{\mathrm{relative}}$ in **eqn (17)**. When all J values are considered the extent of the significant part of each P- and/or R-branch for every sub-band is roughly 12 cm^{-1} with over 100 individual rotational lines. The bottom panel shows part of the R-branch of the pure rotational (a-type) spectrum of NCNCS covering J values from 34 to 116. It is thus an enormous challenge to observe and resolve such a complex and complicated spectrum, particularly considering that the predicted band intensity for the large amplitude CNC bending mode is calculated to be of the order of only 4 km/mole. This is why we have taken the project to the Canadian Light Source [24].

Figure 7 displays the information in **Fig. 6 (top panel)**, dispersed to reveal sets of sub-bands for each v_b. The selection rules follow $\Delta K_\mathrm{a} = 0$, $\Delta v_\mathrm{b} = 1$ and $\Delta J = \pm 1$, just as for a small-amplitude vibrational spectrum. The location of the various K_a sub-bands, however, and the progression of $K_\mathrm{a} = 0$ sub-bands with v_b

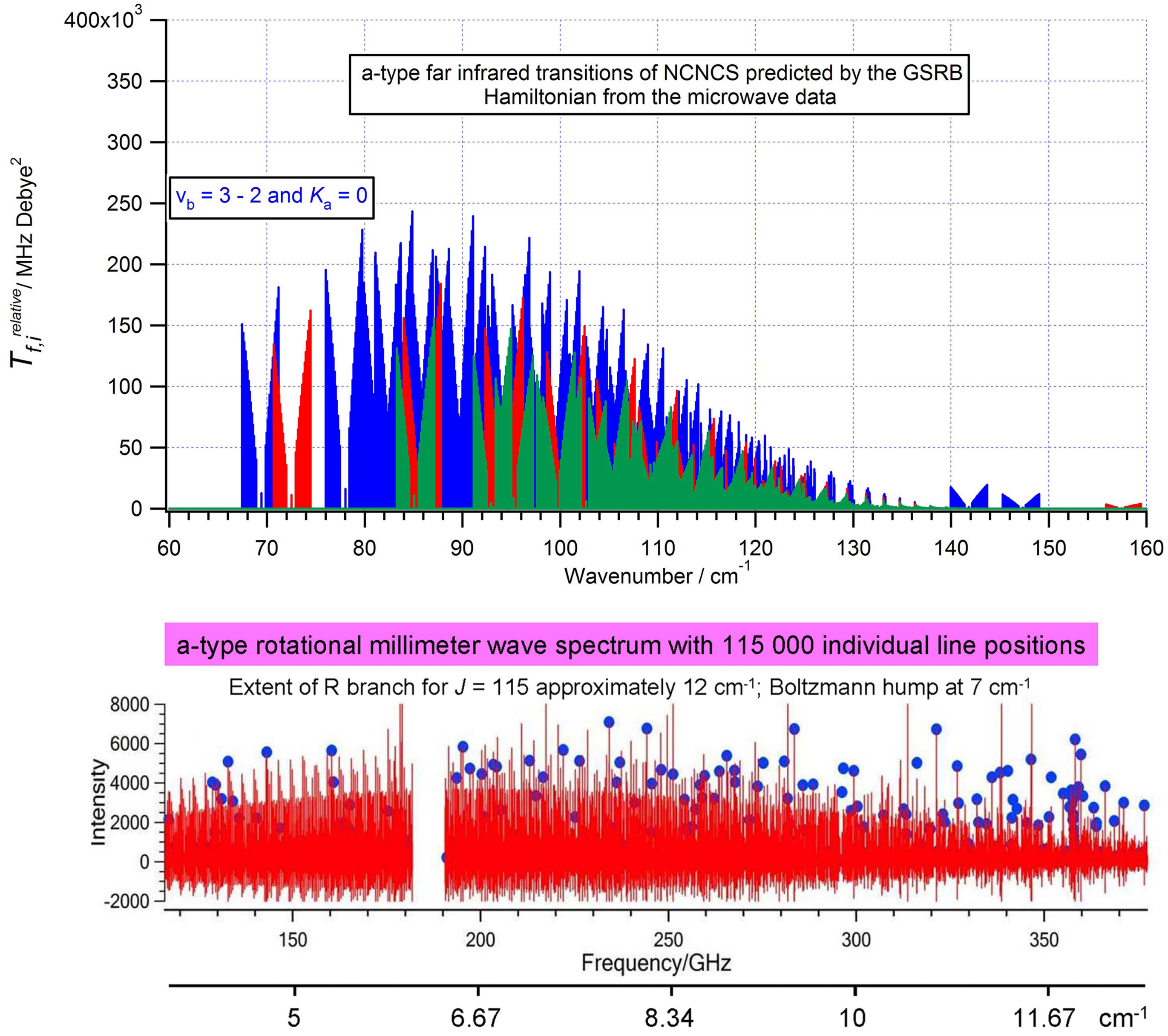

FIG. 6: The top panel shows the superposition of the predicted a-type parallel sub-bands for the large-amplitude bending mode ν_7 for NCNCS. This means that the a-type band system is spread over a wavenumber range of roughly 60 cm^{-1}. The stick-spectrum shows transitions for $\Delta K_a = 0$ and $\Delta v_b = +1$. The range of v_b values is limited to $v_b = 5$; this includes most of the expected intensity. The J value is limited to 20, truncating each sub-band well below the Boltzmann hump, but thus allowing the structure of the spectrum to be discerned. The color coding in the top panel is as in the preceding figures. The bottom panel displays the experimental R-branch millimeter wave pure rotational spectrum of NCNCS from Ref. [2] for $J = 34$ to 115 indicating the full extent of each sub-band to be approximately 12 cm^{-1}; the Boltzmann hump occurs around 7 cm^{-1} for $J \sim 55 - 60$. The lines marked with blue dots are SO_2 calibration lines.

bands clearly reflect the effects of monodromy on the ro-vibrational energy level pattern.

3.3 The b-type spectrum of NCNCS in the THz and Far-Infrared region

We can expect pure rotational b-type transitions throughout the entire THz spectral region as shown in **Figs. 8 to 11**. Our predicted intensities indicate that the b-type sub-bands of the perpendicular component of the

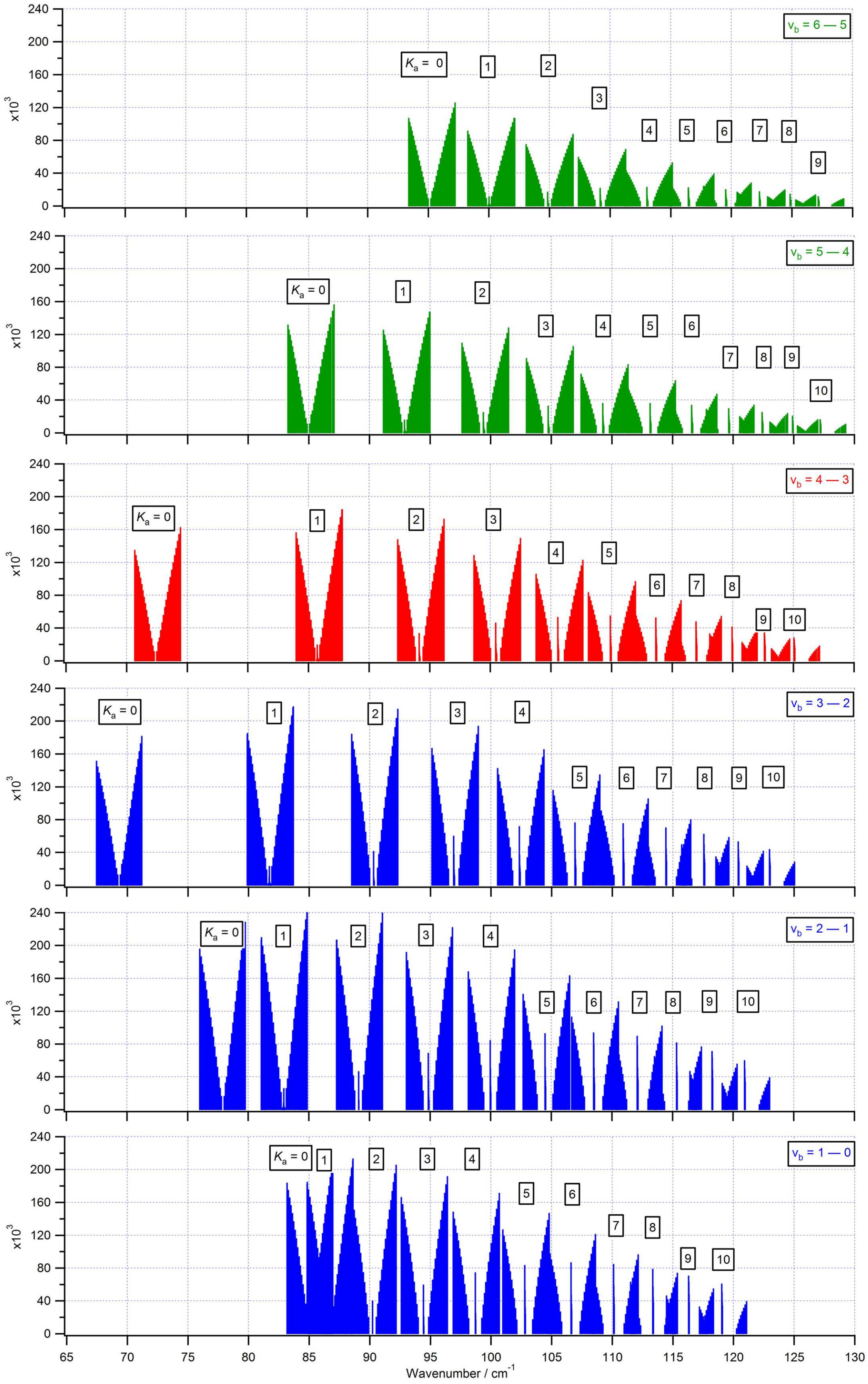

FIG. 7: Calculated sub-bands of the a-type spectrum of ν_7 of NCNCS shown in **Fig. 6 (top)** grouped by v_b with color coding as in previous figure. The a-type sub-bands exhibit weak central Q-branches and P- and R-branches limited to $J \leq 20$. The positions of the origins of the various K_a sub-bands as a function of v_b are a clear manifestation of the effects of quantum monodromy mapped from the energy-momentum map given in **Fig. 2** into the spectrum.

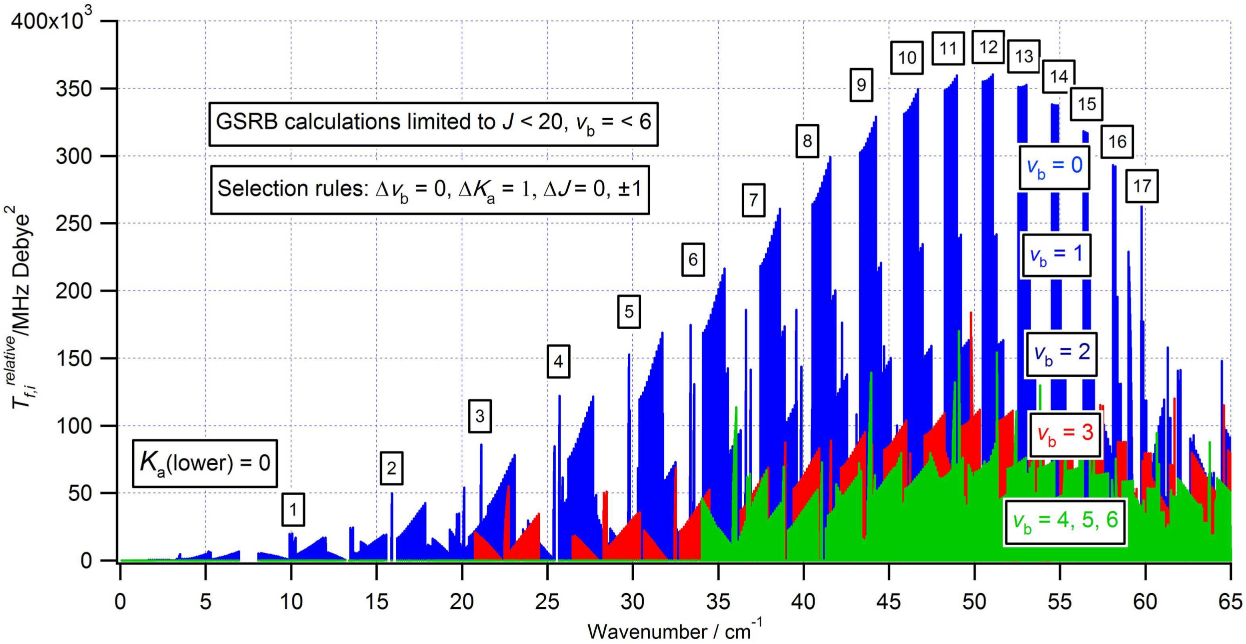

FIG. 8: The b-type rotational spectrum of NCNCS in the THz region as predicted by calculations using the GSRB Hamiltonian. The transitions shown encompass rotational quantum numbers $J \leq 20$ and vibrational quantum numbers $v_\mathrm{b} \leq 6$. Therefore the K_a Boltzmann hump occurs around $K_\mathrm{a} = 12$.

ν_7 band system are similar to those of the parallel component.

The predicted superposition of the rotational b-type sub-bands for $v_\mathrm{b} \leq 6$ is shown in **Fig. 8** and is more unexpected than the respective a-type component and presents a greater challenge for spectroscopic assignment in this difficult THz spectral region. **Figure. 9** is the b-type analogue to **Fig. 7** for the a-type transitions. Here, again, the transitions have been dispersed to show the sub-bands individually for each vibrational transition. In **Fig. 7** it was mainly the positions of the a-type low K_a sub-bands which shifted. Here not only does the position of the individual b-type sub-bands shift but the form of these bands changes as well.

A careful inspection of **Fig. 9** allows one to follow the evolution of the positions of the sub-band positions with v_b. This evolution is more evident if one first examines **Fig. 10** which shows only Delta $K_\mathrm{a} = -1$ transitions from the $v_\mathrm{b} = 1 \leftarrow 0$ transitions in the bottom panel of **Fig. 9**. In **Fig. 10** these transitions are further disbursed by the value of K_a. These sub-bands initially shift to lower frequency with increased K_a, before shifting higher for $K_\mathrm{a} > 3$. Such a reversal is called a “band head”. Returning to **Fig. 9** one can discern that for $v_\mathrm{b} \geq 2$ the Delta $K_\mathrm{a} = -1$ sub-bands completely invert, heading to higher frequency already from the first transition at $K_\mathrm{a} = 1$. The deviation from standard band forms of both linear and bent molecules presents a totally new type of transition band system. As far as we know the formation of a K_a band head not caused by a perturbing resonance has never been described in the literature.

A summary of the above expectations is presented in **Fig. 11**, showing the stick spectrum of all predicted parallel and perpendicular pure rotational and ro-vibrational FIR sub-bands. Similar sub-band structure is to be expected for each of the small-amplitude vibrational bands, though less extended. The result shows that dense absorption should be found from about 20 to 200 cm^{-1} with little obvious structure, but with sufficient spectral resolution and intensity, the spectrum could be assigned. However, we should keep in mind that the ν_7 band system has only a predicted total band intensity of 4 km/mol (see **Table I**).

Fitting the GSRB to the pure a-type rotational spectrum shown in **Fig. 6 (bottom panel)** provided the empirical constants used to make the predictions shown in **Figs. 6 - 11**. The calculated version of the low-J part of that spectrum is the small sub-band below 2 cm^{-1} in the far left hand side of the top and bottom panels of **Fig. 11**. Fully extended the transitions used in the fitting only extend this band to roughly 10 cm^{-1} on **Fig. 11** - all the rest is prediction.

4. THE FAR INFRARED BEAMLINE AT THE CANADIAN LIGHT SOURCE

In the previous section we described the prediction for the ro-vibrational transitions of NCNCS. The question then became where and how to measure this spectrum

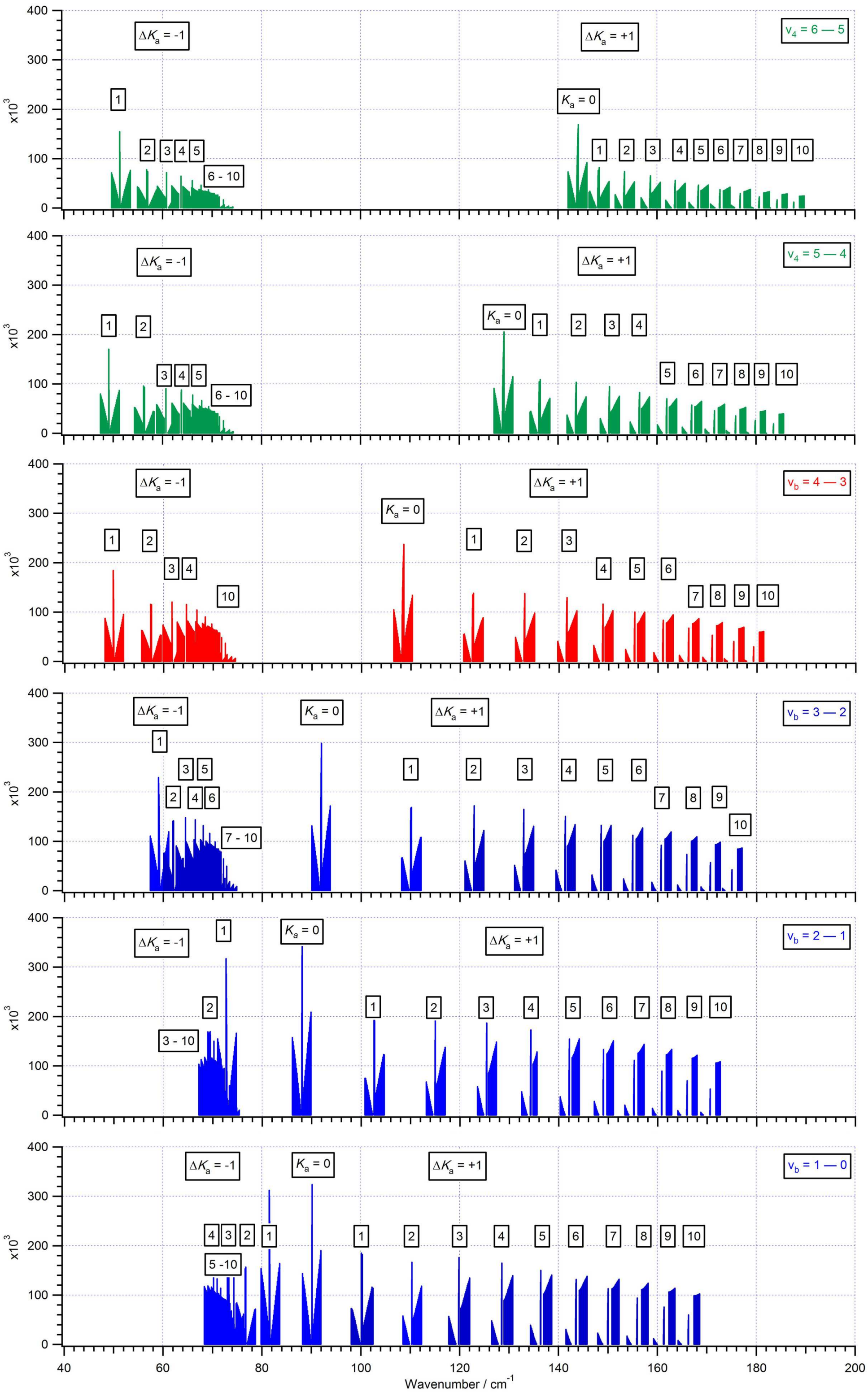

FIG. 9: The b-type perpendicular component of the CNC large-amplitude bending mode of NCNCS with the selection rule $\Delta v_{\mathrm{b}} = 1$. The band system consists of sub-bands for $\Delta K_{\mathrm{a}} = -1$ and $\Delta K_{\mathrm{a}} = +1$ for the fundamental and first five hot bands. The calculated transitions shown were limited to $J \leq 10$ and $K_{\mathrm{a}} \leq 10$. The color coding is the same as in previous figures.

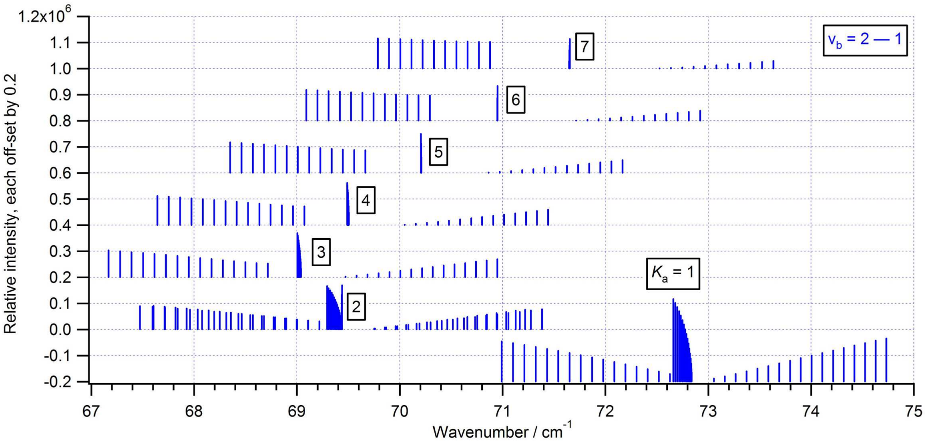

FIG. 10: Expansion of the first b-type hot band. From **Fig. 9** we see that the $\Delta K_\mathrm{a} = -1$, $v_b = 2 \leftarrow 1$ transitions of the ν_7 of NCNCS form a K_a band head which at higher v_b values evolves into a complete inversion of the K_a sequence. structures. This again must be considered a robust manifestation of quantum monodromy in the NCNCS energy-momentum map, the effect of which should be observable in the far-infrared spectrum.

[24–26]. Here we describe why the project was taken to the Canadian Light Source. The background information we provide is at a level we believe is useful to the user community, but is not generally known to chemists or, indeed, even many physicists. Understanding the various aspects of a synchrotron facility allows the user to make decisions regarding the optimal use of a FIR synchrotron beamline for a given experiment like the one proposed and discussed in this work.

A full explanation of synchrotron physics would be far beyond the scope of this paper. There are several good books and papers for those who wish to pursue a greater understanding of the subject [27–30]. Herein, we will endeavour to describe the basic principles behind the production of synchrotron radiation, in a manner understandable to the non-physicist. To those well versed in this physics we beg your indulgence. We will limit our discussion to the response of electrons to bending magnets as they are the primary source of infrared radiation at synchrotrons.

4.1 A brief history of synchrotrons

Though theories about synchrotron radiation go back further [31], the first experimental evidence of synchrotron radiation was found in 1946 by Dr. John Burnett while testing GE's 100-MeV betatron [32]. While synchrotron radiation itself was not observed at this time, the energy losses observed were in accord with the predicted losses due to synchrotron radiation. The first actual observation of synchrotron radiation was made at GE on a 70 MeV electron synchrotron in 1947 [33]. This led to efforts by the GE group and others to characterize synchrotron radiation. The first experimental program exploiting synchrotron radiation would not arise until 1961 at the National Bureau of Standards. This led to the development of facilities to use synchrotron radiation around the world. These facilities were what are now called "First Generation Sources". The were characterized by the fact that they were designed primarily for high-energy particle physics and the use of synchrotron radiation for experiments was mostly done parasitically. The first storage ring specifically designed for the production of synchrotron radiation or "Second Generation Source" opened at Daresbury, UK in 1981. This was followed by a number of rings around the world. The advance that led to third generation sources (of which the Canadian Light Source is an example) was to design rings for high brightness, the first of which was the European Synchrotron Radiation Facility (ERSF) located in Grenoble, France. Many other third generation sources followed and new ones are currently being built. While Free Electron Lasers (FELs) are often referred to as fourth generation sources, most agree that FELs are sufficiently different from synchrotron storage rings, both in design and use, that they are not a replacement for third generation sources, but should be considered as a new line of development. This very truncated history of synchrotron radiation is derived from a number of excellent reviews available in the literature [31, 34].

Further to the history of synchrotron radiation, it is relevant to mention the history of high spectral resolution infrared beamlines (generally used and referred to as Far-Infrared Beamlines) as it is this type of beamline that was used for the research discussed in this paper. Here we draw on the article by A.R.W. McKellar [24], which offers an excellent review of high-resolution infrared spectroscopy at synchrotron sources. While gas phase infrared spectra had been recorded at synchrotrons as early as 1985, it was not until the mid 90's that a ded-

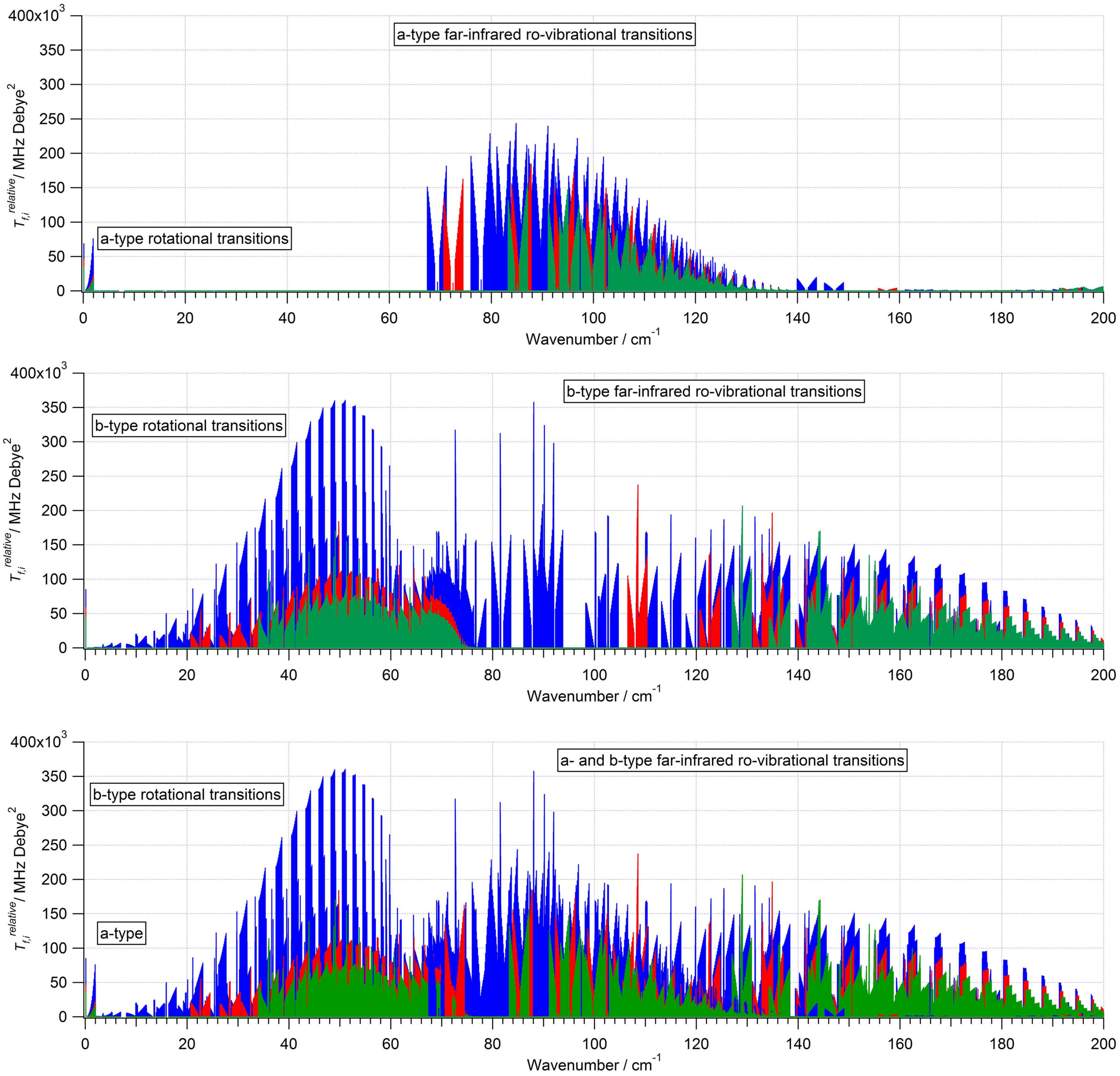

FIG. 11: The top panel shows all predicted a-type parallel sub-bands for the CNC in-plane large amplitude bending mode ν_7 for NCNCS. The middle panel displays all predicted b-type perpendicular sub-bands including $\Delta v_\mathrm{b} = 0, 1, 2, 3$ transitions as indicated in **Fig. 5**. In the bottom panel the superposition of all a-type (see **Fig. 7**) and b-type transitions (see **Fig. 8** and **Fig. 9**) displays the entire hybrid band system of the large-amplitude bending mode ν_7 for a limited range of J and K_a values. This means an enormous number of weak THz- and/or FIR ro-vibrational transitions if we include the fully extended P-, Q- and R-branches in a spectral range of roughly 130 cm^{-1} centered around 100 cm^{-1}. This hybrid band system has only a calculated total band intensity of 4 km/mol (see **Table I**).

icated beamline was built to take advantage of the high brightness of a synchrotron for high resolution infrared spectroscopy [35]. Beamline 73 at MAX I was built by Bengt Nelander, with the first publication of his results appearing in 1995 [36]. This was followed by the SIRLOIN beamline at LURE [37], for which the first published results appeared in 2001. It is the work of these two pioneering groups that lead to the construction of a number of beamlines around the world that are dedicated to high resolution infrared spectroscopy. Arguably the first of these beamlines was the Far-Infrared Beamline at the Canadian Light Source which started operation in 2005, with its first publications appearing in 2007 [38]. Both the AILES beamline at SOLEIL and the far-ir and high resolution FTIR beamline at the Australian Synchrotron were being constructed around the same time with their first publications appearing 2010 [39] and 2008 [40], respectively. Since then a number of other facilities have been built, though there exist only seven such facilities, of which we are aware.

4.2 The anatomy of a synchrotron

A synchrotron is a particle accelerator, generally accelerating electrons. The first stage is an electron gun, followed by a linear accelerator which accelerates bunches of electrons. These are then injected into a booster ring which uses a radio frequency field to further accelerate the electrons to the desired velocity (very near the speed of light). Quadrupole magnets are used to direct the electrons in a circular path and to focus them into a thin beam. The magnets used to direct the electrons into a circular path are called bending magnets and the focussing is done by quadrupole magnets. Once at the desired speed the electrons are injected into the larger storage ring. The storage ring uses similar components to the booster ring to maintain the velocity of the electrons. Devices placed (inserted) in the straight sections between the bending magnets are called *insertion devices.* In Third Generation rings the insertion devices are typically wigglers or undulators, which cause the electron beam to wiggle or undulate as it passes through them, thereby producing intense electromagnetic radiation.

4.3 The physics of synchrotron radiation

The following basic explanation of the generation of light from a synchrotron borrows from The Feynman Lectures [27] on Physics and Kwang-Je Kim's Characteristics of Synchrotron Radiation [29], both of which we recommend for further reading. We limit our discussion to electrons as these are the particles in the synchrotron beam at the CLS. We begin by considering only a single electron, despite the fact that in synchrotrons electrons circulate in groups termed *bunches.* For the generation of synchrotron radiation it is the charge of an electron, $-e$, (elementary charge $e = 1.602\,177\,33(49)\times10^{-19}$ Coulomb), that is important. In a static picture the magnitude of the electric field produced by an electron is given by Coulombs Law,

$$|\vec{\boldsymbol{E}}| = \frac{e}{4\pi\varepsilon_0 r^2} \tag{20}$$

where r is the distance between the electron and the observer and ε_o is the permittivity of vacuum or free space. Synchrotrons produce electromagnetic radiation by accelerating electrons. **Eqn (20)** does not take into account the motion of the electron. Accounting for the time dependence of the position of the electron leads to the time-dependent equation for the electric field [27],

$$\vec{\boldsymbol{E}} = \frac{e}{4\pi\varepsilon_0}\left[\frac{\hat{\boldsymbol{e}}_{r'}}{r'^2} + \frac{r'}{c_0}\frac{d}{dt}\left(\frac{\hat{\boldsymbol{e}}_{r'}}{r'^2}\right) + \frac{1}{{c_0}^2}\frac{d^2}{dt^2}\hat{\boldsymbol{e}}_{r'}\right], \tag{21}$$

and, for completeness, the magnetic field,

$$\vec{\boldsymbol{B}} = -\hat{\boldsymbol{e}}_{r'} \times \frac{\vec{\boldsymbol{E}}}{c_0}, \tag{22}$$

where c_0 is the speed of light in vacuum.

It is only the electric field strength, **eqn (21)**, that is needed for our discussion. A prime ($'$) is placed on r and other quantities in **eqn (21)** to indicate that they are relative to what is called *retarded time.* The introduction of the concept of retarded time is necessary because the electric field only propagates at the speed of light. Due to the time it takes for the electric field to propagate to the observer, what the observer sees at a particular moment t is the result of the position of the charge at some point in the past, a time r'/c_0 before t. That is, r' is the distance between the observer and the electron at the time when the electric field currently experienced by the observer emanated from the electron, not the separation between the observer and electron at the current time. As we shall see it is precisely the difference between the retarded time and the observer's time that leads to the particular form of synchrotron radiation. In **eqn (21)** $\hat{\boldsymbol{e}}_{r'}$ is a unit vector pointing from the observer to where the electron was when the currently experienced field left the electron. That is, $\hat{\boldsymbol{e}}_{r'}$ again refers to a quantity relative to retarded time. This vector is shown in **Fig. 12**. The first term in **eqn (21)** represents the electrostatic field due to the charge of the emitting electron. This field decreases as the square of r' and therefore may be neglected in the far-field limit. In this limit the second term of **eqn (21)** also becomes negligible. It is the third term that is important in the generation of radiation that can propagate into the far regions and we therefore need only consider the electric field arising from it,

$$\vec{\boldsymbol{E}} = \frac{e}{4\pi\varepsilon_0}\frac{1}{{c_0}^2}\frac{d^2}{dt^2}\hat{\boldsymbol{e}}_{r'}. \tag{23}$$

Thus it is the acceleration of the unit vector $\hat{\boldsymbol{e}}_{r'}$ in **eqn (23)** that leads to the generation of radiation. Consider an electron moving in a circular orbit in the X, Z plane in a Cartesian coordinate system (see **Fig. 12**). In the present context the lower part of this circle this would correspond to the path of the electron as it moves through the bending magnet, which at the CLS is the source of the far-infrared radiation and has a radius of curvature

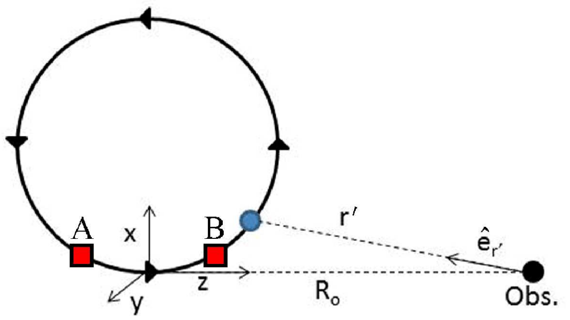

FIG. 12: Trajectory of an electron moving in a circular path. r' is the distance from the observer to the location of the electron at the retarded time (τ). $\hat{\boldsymbol{e}}_{r'}$ is the unit vector directed from the observer to the electron. R_0 is the distance from the origin of the X, Y, Z coordinate system to the observer (Obs.). **A** and **B** are points on either side of the bottom of the circle.

of 7.143 m. Since $\hat{\boldsymbol{e}}_{r'}$ only has components in the X, Z plane we only need consider $x(t)$ and $z(t)$, the instantaneous position in the X, Z plane of the emitting electron. The only possible change to a unit vector such as $\hat{\boldsymbol{e}}_{r'}$ is in a direction perpendicular to itself. When the electron is in the lower part of the circle in **Fig. 12** $\hat{\boldsymbol{e}}_{r'}$ is essentially in the $-z$ direction so any significant change in it is in the transverse direction, the x-direction. From the geometry of **Fig. 12** it is clear that such a change is almost entirely due to the motion of the electron in the x-direction. With the observer far enough away (i.e. R_0 much larger than the radius of the circle) the transverse component of $\hat{\boldsymbol{e}}_{r'}$ is x'/r', while the parallel (z-component) is approximately constant with a value of ≈ -1. We can therefore evaluate,

$$\frac{d\hat{\boldsymbol{e}}_{r'}}{dt} \approx \frac{d}{dt}\left(\frac{x'}{r'}\right)\hat{x} = \left(\frac{1}{r'}\frac{dx'}{dt} - \frac{x'}{r'^2}\frac{dr'}{dt}\right)\hat{x} \tag{24}$$

Since R_0 is much larger than the radius of the circle, $r' \approx R_0 - z' \approx R_0$, and **eqn (23)** can be further approximated as,

$$\frac{d\hat{\boldsymbol{e}}_{r'}}{dt} \approx \left(\frac{1}{R_0}\frac{dx'}{dt} + \frac{x'}{R_0^2}\frac{dz'}{dt}\right)\hat{x} = \frac{1}{R_0}\left(\frac{dx'}{dt} + \frac{x'}{R_0}\frac{dz'}{dt}\right)\hat{x}' \tag{25}$$

where $\hat{x}$ is a unit vector pointing in the $+x$ direction shown on **Fig. 12**. Since $x' \ll R_0$ the second term in parentheses can be neglected relative to the first term and we finally obtain an approximate expression for the electric field at the location of the observers',

$$\begin{aligned}\vec{\boldsymbol{E}} &= \frac{e}{4\pi\varepsilon_0}\frac{1}{c_0{}^2}\frac{d^2}{dt^2}\hat{\boldsymbol{e}}_{r'}\\ &= \frac{e}{4\pi\varepsilon_0}\frac{1}{c_0{}^2}\frac{d}{dt}\left(\frac{1}{R_0}\frac{dx'}{dt}\hat{x}\right)\\ &= \frac{e}{4\pi\varepsilon_0}\frac{1}{c_0{}^2 R_0}\frac{d^2x'}{dt^2}\hat{x}.\end{aligned} \tag{26}$$

We see that in this level of approximation the observed electric field depends on the acceleration of the electron in the transverse, or x, direction.

It is trivial to plot the true motion of the electron along the X-axis, $x(t)$, as a function of non-retarded time - it is a pure sinusoid curve whose frequency is directly proportional to the velocity of the electron. With small enough velocities compared to the speed of light the plot of $x'(t)$, that is x as seen by the observer will be essentially identical to $x(t)$. For the motion of an electron through the bending magnets of the CLS this is pretty much the case if the velocity is $0.01 \times c_0$. Thus the plot in **Fig. 13a** can be thought of as either $x'(t)$ or $x(t)$. The result is that the observed electric field shown in **Fig. 13c** is also essentially unaffected by the finite propagation speed of the electric field and so also takes a very sinusoidal form.

If we consider the 2.9 GeV electrons as they pass through the 7.143 m radius curve through the bending magnets at the CLS the situation is dramatically different. To plot this we must carefully account for retarded time. As stated above, from observers point of view, observations are delayed by the time r'/c_0 that it takes for the instantaneous field of the electron to travel the distance r' to the observer. *Retarded time*, denoted τ, is the time the electric field begins to propagate to the observer. The relationship between τ and the observers time is obviously $t = \tau + r'/c_0$. Again using the approximation $r' \approx R_0 - z'$ we obtain

$$t \approx \tau + \frac{R_0}{c_0} - \frac{z'}{c_0}. \tag{27}$$

The R_0/c_0 term is constant and only affects the relative starting times of clocks and we can ignore it to find the approximate, but useful, relationship between retarded time and observer's time,

$$t \approx \tau - \frac{z'}{c_0}. \tag{28}$$

Taking this into account we can plot the apparent position, $x'(t)$, of the electron as seen by the observer. This is done in **Fig. 13b**. Due to the second derivative in **eqn 26** the cusp in the apparent position of the electron as a function of time gives an enormous negative result for the electric field strength. This can be seen in **Fig. 13d** which shows the electric field seen by the observer from a single electron in the bending magnet at the CLS. (If the electron where travelling at the speed of light the cusp in **Fig. 13b** would be infinitely sharp and therefore the resulting electric field would be infinite as well.)

What is actually happening here? Due to the finite speed of propagation of the electric field the observer has to wait longer to feel the electric field from when the electron is at point **A** than from when it is at point **B**. This longer lag of the field from the first point compared to that at the second point means that the time difference between the observations of these two electric fields is compressed in the observers frame compared the time taken for the electron to move between points **A** and **B**. That is, although the signal from **A** still arrives before that from **B**, it arrives relatively later than that from **B** and so the interval perceived by the observer between these two signals is shortened. As the speed of the electron approaches that of light this compression becomes extreme, as seen by comparing **Fig. 13b** and **Fig. 13d**.

A Fourier transform of the electric field due to a low-speed electron, as shown in **Fig. 13c**, would simply give a single frequency of radiation at the revolution frequency. With the very sharp feature in **Fig. 13d** the Fourier transform would instead give a very broad spectrum, covering a large range of frequency from far-infrared to hard x-rays. The maximum of this spectrum will be near the critical angular frequency, $\omega_c = 2\pi\nu_c$, which for a bending magnet is,

$$\omega_c = \frac{3\gamma^3 c_0}{2\rho}. \tag{29}$$

Here ρ is the bend radius (the radius of the circle in **Fig. 12**) and γ is the usual relativistic factor which can also be defined as the ratio of the total relativistic energy, E_e, of the electron to its rest energy,

$$\gamma = \frac{\mathrm{E}_e}{m_e c_0^2}. \tag{30}$$

where m_e is the rest mass of the electron [29]. At the relativistic energies of an electron in a synchrotron the total relativistic energy and the kinetic energy are nearly equal, differing only in the rest-energy of the electron, $m_e c_0^2$, that is by a difference of one in the value of γ. Converting **eqn 30** to practical units and with E_e given in GeV we have,

$$\gamma = \frac{1957}{\mathrm{GeV}} \times \mathrm{E}_e \left(\approx \frac{1957}{\mathrm{GeV}} \times 2.9\,\mathrm{GeV} \,=\, 5675\right), \tag{31}$$

for the CLS. For the bending magnets at the CLS the critical frequency corresponds to the X-ray region, around 7.57 eV (or wavelength of around 1.6 Å).

The basic overview of the physics behind synchrotron radiation given above is an idealized model. One limitation is that the observer was represented as a single point. This is unrealistic and for the case of infrared radiation leaves out several important points related to the collection of the radiation from the synchrotron. The electron path in a synchrotron's storage ring is not actually a circle. Instead it is made up of a number of bending magnets connected by long straight sections. Furthermore, synchrotrons do not accelerate single electrons at a time. Instead they accelerate many electrons in groups called bunches. In a storage ring there can be more than one bunch at a time. The synchrotron current is determined by the number of bunches, the number of electrons in each bunch, and the orbital frequency (or speed) of the bunches. The amount of radiation produced varies roughly linearly with the current. The emitted radiation is then collected through ports. The observer only "sees" the electrons as they pass through the ports field of view. At the Far-Infrared Beamline at the CLS the radiation used is that produced as the electrons pass through a bending magnet and the port is therefore placed in front of that magnet. The motion of the electron as it passes through the bending magnet is equivalent to the motion at the bottom of the circle in **Fig. 12**. This is what we described above and is what leads to the observed radiation shown by the sharp feature in the center of **Fig. 13d**.

Generalizing from a single-point observer we now consider an observer of finite size, spread out in the X, Y plane, which would be the cross-section plane of a sample. (Spread in the Z-direction is not of interest for the present simplified discussion). In **Fig. 14**, **b** is the instantaneous direction of the electron. For points off-axis in the X, Y plane the geometry is somewhat different from the on-axis direction considered above and we must consider the shape of the beam of radiation emitted from the electron, as suggested in **Fig. 14**. It turns out that for small angles, ϕ, off the beam axis **b** the effect of this different geometry can be described by a single factor, the scale-change factor, (κ), the factor by which the observer time, t, differs from the retarded time, τ. κ has the value

$$\kappa \approx \frac{1}{2}\Big(\frac{1}{\gamma^2} + \phi^2\Big);\ \phi << 1. \tag{32}$$

Above we assumed that the angle between the observer and the direction of the electron motion was $\phi = 0$. This value gives $\kappa = 1/(2\gamma^2)$, a very small value, implying a strong time compression and thus the generation of strong synchrotron radiation. However, as the angle ϕ increases κ very quickly becomes larger with the result that the time compression is reduced off axis, and the intensity of the synchrotron radiation quickly drops. This means that the synchrotron beam has a small divergence angle, and consequently is very narrow. As an electron moves around the ring this narrow beam of synchrotron radiation can be compared to a searchlight sweeping through the X, Z plane, occasionally impinging upon ports and entering experimental areas.

There is another important point with regard to infrared radiation. For a high-energy ring the radiation at small divergent angles, ϕ, is mainly in the x-ray region. However, at higher ϕ the radiation is in the infrared region. Therefore most infrared beamlines only collect the radiation at higher angles from the X, Z plane. This is done by either using a mirror with a thin *beamstop* covering its center or by using a mirror with a slot cut out of the center to allow the x-rays to pass through. **Eqn 29** unfortunately means that the off-axis location of the infrared radiation from a high-energy synchrotron is

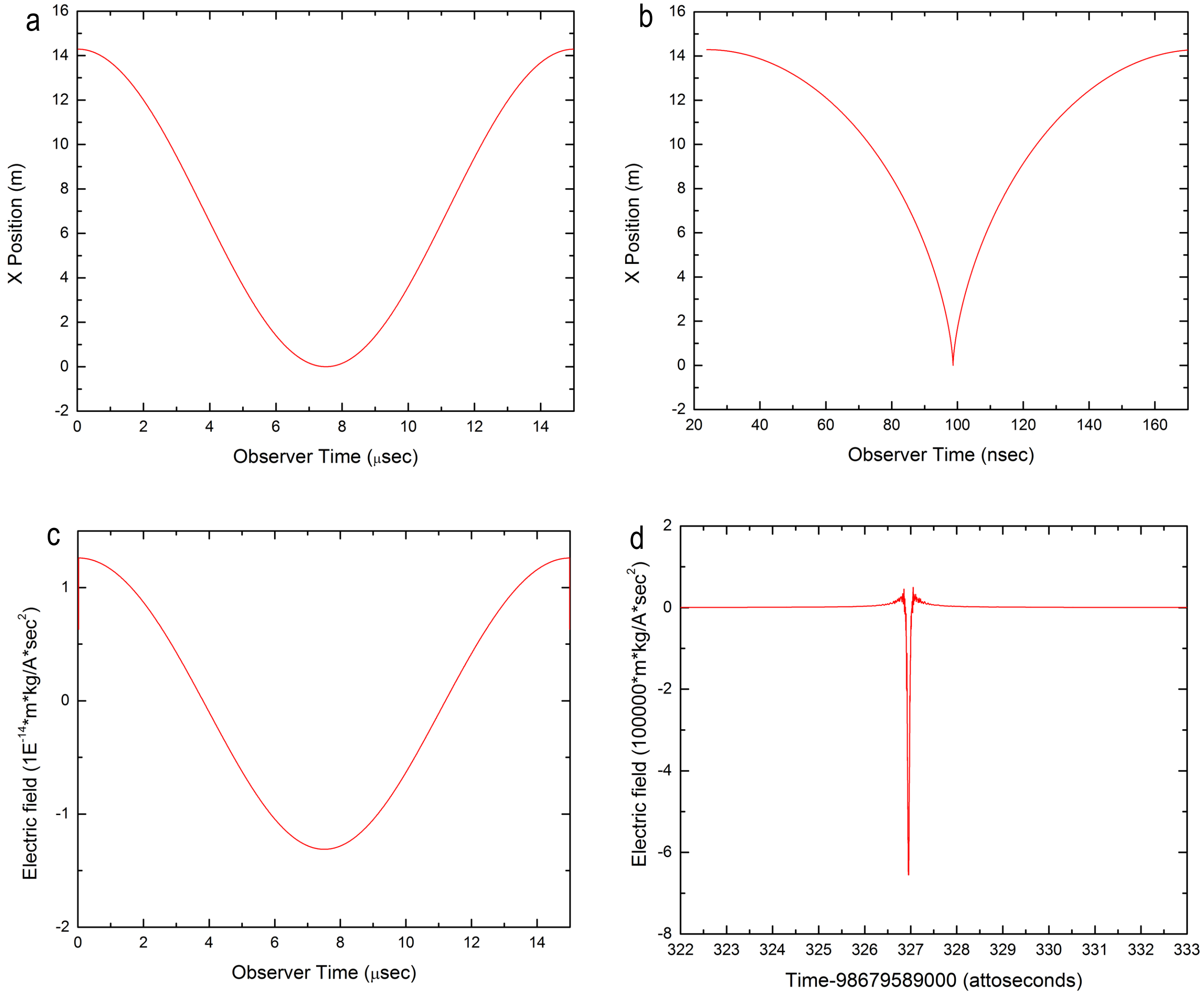

FIG. 13: **Panel 13a**: X-position of the electron as a function of observer time t when moving at $0.01 \times c_0$ in a circular path of radius of 7.143 m in the X, Z plane. **Panel 13b**: X-position of electron a function of observer time t when moving at $0.999999986 \times c_0$ (as in the CLS) in a circular path of radius of 7.143 m in the X, Z plane. Notice that this figure takes on a hypocycloid rather than the sinusoidal shape seen in panel 13a. **Panel 13c**: Electric field strength of electron as observed by the observer (see **Fig. 12**) as a function of observer time t for an electron moving at $0.01 \times c_0$ in a circular path with a radius of 7.143 m in the X, Z plane. **Panel 13d**: Electric field strength of electron as observed by the observer as a function of observer time t when moving at $0.999999986 \times c_0$ in a circular path of radius of 7.143 m in the X, Z plane. Note: the vertical scales in the panels **c** and **d** are in electric field strength.

not as intense as shorter wavelength radiation. In fact it is generally not significantly more intense than the infrared radiation produced from a conventional source. A particular case which is an exception to this difficulty of lower intensity is the generation of intense coherent synchrotron radiation [41]. That, however, is a special case not related to the current work.

This then begs the question of what advantage there is in using infrared synchrotron radiation. For most conventional uses of infrared spectroscopy the answer is that there is no advantage. However, for high resolution infrared spectroscopy, whether you are referring to either spatial or spectral resolution, there is a significant advantage due to the inherent brightness of the synchrotron beam. While the intensity of the infrared light radiated by the synchrotron is not greater than that available from a conventional source, the synchrotron light is radiated from a much smaller area and angle, allowing the light

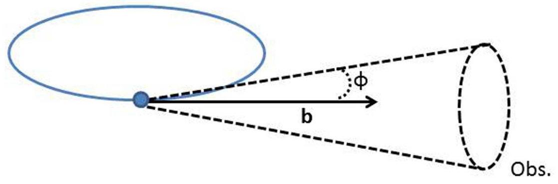

FIG. 14: The opening angle of a synchrotron light beam. **b** is the instantaneous direction of the electron motion and ϕ is the angle between the outer edge of the observer and **b**.

to be focussed to a much smaller spot size. The advantage of this for infrared microscopy, which requires high spatial resolution, is obvious. However, the advantage for high spectral resolution is not so obvious until one recognizes that to achieve high spectral resolution one requires small apertures to ensure that there is less of a spread in path length differences due to geometric effects. Therefore the higher the spectral resolution the smaller the aperture must be. When using a conventional source most of the light will be rejected by the aperture. Since the light from a synchrotron already has a very narrow spatial profile a much higher proportion of the light can be passed through the aperture. This can result in higher throughput and therefore higher signal-to-noise ratios, so that high quality spectra can be collected using a synchrotron in a fraction of the time required using a conventional source. In many cases it would simply not be practical to acquire spectra using a conventional radiation source to obtain the signal-to-noise ratios achievable by a synchrotron.

4.4 The Far-Infrared Beamline at the Canadian Light Source (CLS)

For a complete understanding of how high-resolution infrared spectroscopy is achieved at a synchrotron it is necessary to briefly describe a beamline in more detail. While all such beamlines are similar they do differ in design and performance. Since the research described in this paper was carried out at the Far-Infrared Beamline at the Canadian Light Source (CLS) we will use it as an example. The CLS is a third generation storage ring, with a 171 meter circumference, operating at an energy of 2.9 GeV with a maximum current of 250 mA (seen in **Fig. 15**).

Figure 16 shows the Far-Infrared Beamline at the CLS. Synchrotron radiation is collected from a bending magnet via a slotted flat mirror (as described previously). This mirror is set at a 45 degree angle directing the radiation upward to an elliptical mirror which focusses the radiation through a diamond window, which separates the ultra-high vacuum environment ($\sim 10^{-10}$ Torr) of the storage ring from the rough vacuum ($\sim$ 10^{-2} to 10^{-4} Torr) environment of the beamline. After this a series of elliptical and flat mirrors direct the radiation so that it is focused on the entrance aperture of the spectrometer.

The Far-Infrared Beamline at the CLS is equipped with a Bruker IFS 125HR Fourier transform spectrometer with a maximum optical path difference of 9.4 m, which allows it to achieve resolutions better than 0.00096 cm^{-1} or 28.78 MHz for FWHH. The spectrometer is equipped with a full range of beamsplitters, detectors and internal sources allowing it to operate from 12 cm^{-1} to 20000 cm^{-1}. Typically the synchrotron is only used as a radiation source between 12 cm^{-1} to 1000 cm^{-1} as this is where the synchrotron has a significant advantage over the internal sources. There are a number of specialty sample cells available or under development, but the primary sample cell used is a 2 m White-type multi-pass cell with a maximum pathlength of 72 m. This cell can be cooled to $-80\,^{\circ}$C using a recirculating chiller.

We can demonstrate the advantage of using the synchrotron as a source by comparing the signal-to-noise (S/N) achieved using the synchrotron to that obtained using internal thermal sources. This is done for the highest achievable resolution 0.00096 cm^{-1} where small apertures are needed. When using the required apertures to achieve a resolution of 0.00096 cm^{-1}, the synchrotron provides an advantage over the indicated wavenumber range of between 3 and 20 times in terms of only signal with the greatest advantage observed around $\sim$ 130 cm^{-1}. However, because the synchrotron radiation contains more noise than a thermal source the S/N advantage is lower. **Figures 17**, **18** and **19** show the ratio of the S/N achieved using the synchrotron over the S/N achieved using the appropriate thermal source in the same amount of time, in various spectral regions. In all cases the signal to noise was calculated in 0.2 cm^{-1} steps. In all cases the data has been smoothed using the Savitzky-Golay [42] algorithm, with a 2nd order polynomial function and 25 points to either side of the point in question. It is important to remember that S/N goes as the square root of the number of scans, so that even a modest S/N advantage can provide a significant advantage in the amount of time required to collect a spectrum.

5. CHEMICAL PREPARATIONS OF NCNCS, UNEXPECTED CHALLENGES ENCOUNTERED AND HIGH-RESOLUTION FTIR SPECTROSCOPY

A number of syntheses for NCNCS have been developed to date. Previous work on the pure rotational millimeter wave spectrum at The Ohio State University used the method developed by King and Kroto in 1980 [43], in which a flowing stream of the isomer $S(CN)_2$ was py-

FIG. 15: At the core of the Canadian Light Source are three particle accelerators: an electron linear accelerator (located underground), a booster synchrotron (the inner ring in this photo) and an electron storage ring (hidden in the foreground). The electron storage ring operates at a current of 250 mA with an energy of 2.9 GeV. The long stored beam lifetime has permitted electron re-injection to be reduced to twice per day. The storage ring, with a 171 meter circumference, supports 14 independent beam lines from THz region (about 0.025 eV) to hard X-rays (more than 100 keV).

rolized at 855 °C to produce NCNCS [2]. The pyrolysis produces a plethora of small chemical-sink molecules such as CO_2 and NCCN (and probably CNCN, CS_2, CS, CO, HNCO, HNCS, etc. as well), but most of these molecules did not interfere with the millimeter wave measurements since they either did not possess a permanent electric dipole moment or had negligible vapor pressure at the low temperature maintained at the sample reservoir. Because of the continuous flow of sample through the system, the contaminants were gradually purged from the reservoir. This procedure produced NCNCS absorption lines with a signal-to-noise ratio considerably greater than 1000:1

Alternative syntheses have been described in the literature [44–46], and were either considered or attempted during our experiments at the CLS. For instance, Devore [45] reports that a mixture of silver thiocyanate, AgSCN, with iodine, I_2, will produce NCNCS when heated to more than 400 K. Li, Keong, and Fan used this method in some photochemical laser work on NCNCS [46]. We were unable to produce NCNCS in this manner or by simply heating AgSCN, and indeed this observation has been confirmed by Neidlein and Reuter [44]. However, those same authors reacted the di-potassium salt of N-cyano-imido-dithiocarbonic acid with phosgene in anhydrous methylene chloride and did obtain a solution of NCNCS in CH_2Cl_2. The liquid infrared spectrum revealed an intense band at 2240 cm^{-1} which they assigned to the terminal NC-group in NC-NCS. A broad band system at 1970 cm^{-1} is indicative of the iso-thiocyanate (-NCS) group attached to the nitrile group, while a third absorption band was found at 1105 cm^{-1} which they assigned tentatively to the iso-thiocyanate stretching vibration (see **Table, I**, harmonic potential energy distribution). Comparing these results with results with the gas-phase results for ν_1, ν_2, and ν_3 in **Table I**, we see that Neidlein and Reuter [44] were obviously the first chemists who had the good fortune to synthesize and observe NCNCS in solution.

During the course of our research work, we found that Jin Wang's Ph.D. dissertation from 2007 [12] independently presented a valuable introduction into the generation and the gas-phase infrared spectrum of NCNCS. He supported his work with quantum mechanical calculations which are in good agreement with our early theoretical work given in Ref. [10]. **Table I** reports the positions in wavenumber of Wang's experimental low-resolution infrared features. Since his work has only recently come to our attention, we have not yet attempted his synthesis.

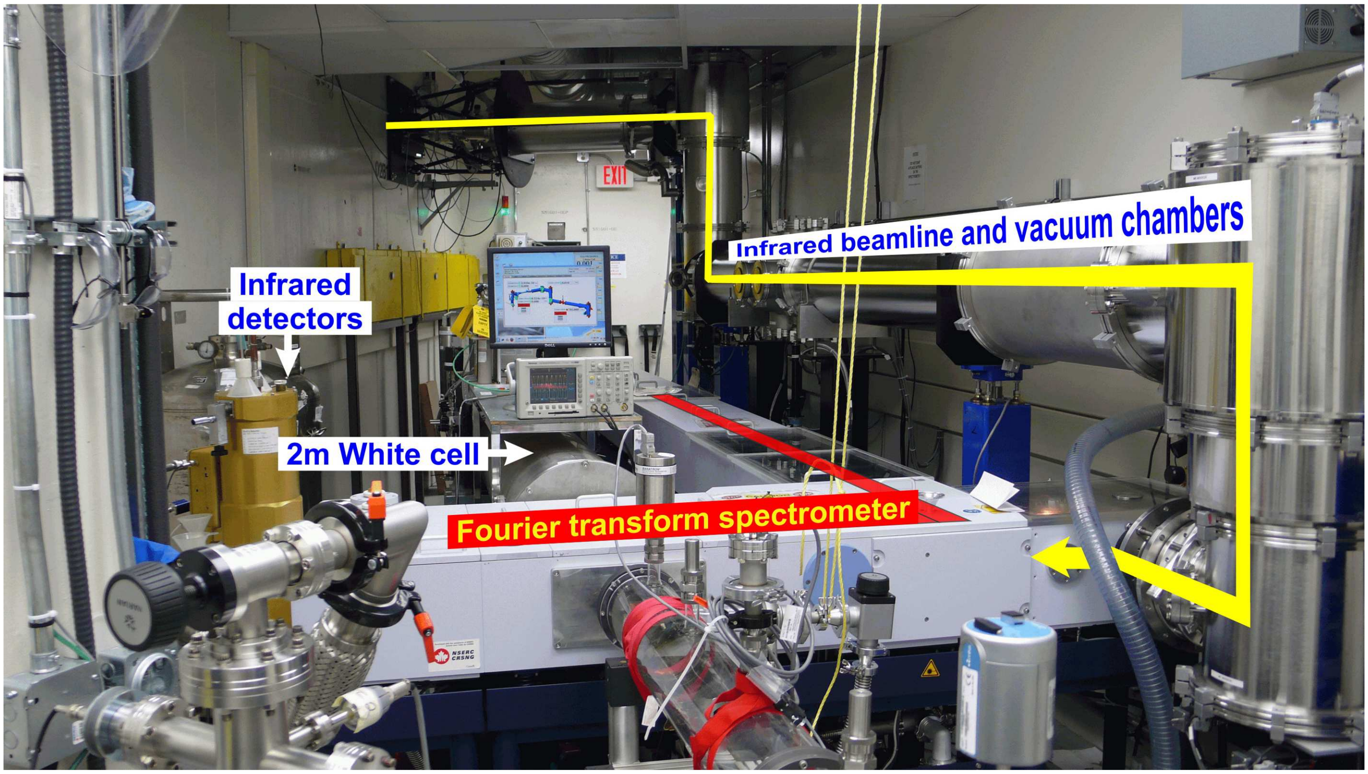

FIG. 16: Inside the hutch of the CLS far-infrared beam line, showing the Bruker IFS125-HR Fourier transform spectrometer, the beam line transfer optics, and the 2m White absorption cell. The chain of mirrors which comprises the beam line collects far-infrared light from the bending magnet section of the electron storage ring through an angular aperture of 55 by 37 milliradians. A diamond window separates the ultra-high vacuum ($\sim 10^{-10}$ Torr) of the storage ring from the rough vacuum ($\sim 10^{-2}$ to 10^{-4} Torr) of the beam line. The infrared light enters the hutch at the upper left and proceeds to the Fourier transform spectrometer via the rather circuitous path shown here.

For all of our experiments conducted at the CLS, we produced NCNCS by the method of King and Kroto [43].

The synthesis was performed in a wet chemistry laboratory at the CLS, which was outfitted with a fume cabinet but essentially no equipment for synthetic chemistry, so a significant amount of laboratory apparatus had to be shipped to the synchrotron facility. In setting it up and using it we have learned how to manage the synthesis under constrained laboratory conditions while at the same time following the required safety rules and restrictions. As a first step, we needed to synthesize SCl_2 [47] since this compound is no longer commercially available in Canada. Following the procedure given by Long and Steele [48], we then used the SCl_2 in the production of $S(CN)_2$ [18], which was pyrolyzed to facilitate its isomerization into NCNCS. All of the relevant experimental details for the syntheses of SCl_2 and $S(CN)_2$, as well as the ro-vibrational analysis of the latter species are described in detail in Ref. [19]. Particulars regarding the pyrolyses performed during each campaign at the CLS will be given in the following sections.

5.1 First measuring campaign May/June 2011 at the CLS: $S(CN)_2$ and NCNCS

The first campaign at the CLS was perhaps the most complex experiment attempted on the Far-Infrared Beamline up to that time. In the initial phase, significant time was expended to configure the wet laboratory for preparation of our sample. The same synthesis that had proven successful at The Ohio State University was employed. The various steps required for one preparation of the precursor molecule, $S(CN)_2$, can be briefly summarized, and are illustrated in **Fig. 20** with photographs taken at the CLS during the experiment. Step 1 shows the synthesis of SCl_2 by reacting ClSSCl with elemental Cl_2. Step 2 depicts the separation of SCl_2 from ClSSCl by distillation. The two liquids, SCl_2 and ClSSCl, can be separated easily due to the large difference in their boiling points, +59.6 °C and +138 °C. Step 3 shows the addition of silver cyanide, AgCN, to the distilled SCl_2, yielding $S(CN)_2$ which can be purified by sublimation as is shown in step 4. The resulting sample was kept under dry ice or liquid nitrogen to prevent its polymerization. Warming it to temperatures between −10 to −5°C produced vapor pressures sufficient for our purposes. In our

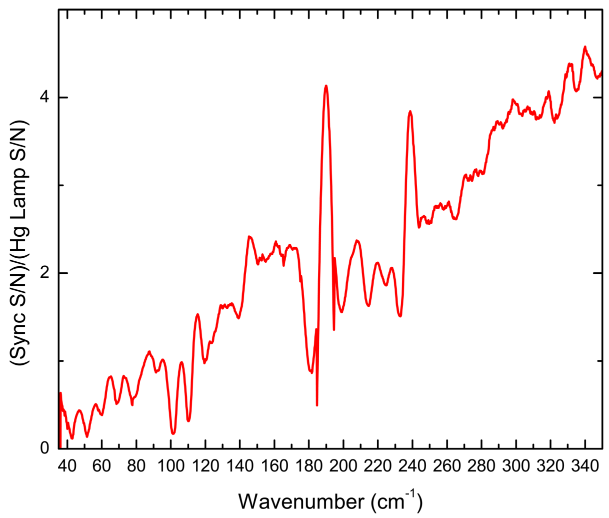

FIG. 17: Ratio of the signal-to-noise achieved using the synchrotron as a source over that achieved using an Hg Lamp in the 35 to 350 cm^{-1} region. Both spectra were collected at a nominal resolution of 0.00096 cm^{-1}, with a 2 mm aperture, a 6 micron mylar beamsplitter, a liquid helium cooled Si bolometer and a gain of 1000×. The synchrotron data was the average of 30 scans collected at a velocity of 30 kHz while the Hg lamp data was the average of 6 scans collected at a velocity of 5 kHz. (Note that interferometer mirror velocities can be measured by the frequency at which the He-Ne interference fringes, used to mark distance along the path of the scanning mirror, are encountered.) The overall collection time for the two data sets was equal. In this case a different velocity where used because a slower velocity favors the Hg lamp as the Si bolometer sensitivity varies inversely with velocity while a higher velocity favors the synchrotron because it shifts mechanical noise outside of the spectral window. See text for details.

first experiments, we successfully obtained the spectrum of the ν_4 bending mode of S(CN)$_2$ and a sequence of associated hot bands, as well as data on the ν_7 and ν_8 fundamentals, the analyses of which have been reported in an earlier publication [19]. The experiments were conducted in a 2 m long White cell with a volume of about 300 litres set for 40 passes. The cell was outfitted with polypropylene windows, and the silicon bolometer was used as a light detector so that a bandpass of about 50-350 cm^{-1} could be achieved. Initially we had concerns that the S(CN)$_2$ sample, left in static conditions at 100-200 mTorr, might decay in a short time due to reactions and collisions with the cell walls, and indeed over the first few hours of the experiment some sample loss was observed. After this, the cell seemed to become conditioned, and the remaining sample remained quite stable over several days, particularly when the cell was cooled to about −5 °C with chilled methanol. After this initial successful experiment, we removed our sample and set up the pyrolysis oven shown in step 5 of **Fig. 20** near the inlet tube to the cell. We arranged for the S(CN)$_2$ vapor to effuse into the White cell, passing first through the pyrolysis oven, which was heated to 855 °C. Inside the oven, the gas was contained in a quartz tube about 3 cm in diameter and filled with coarse quartz chips to maximize its contact with hot surfaces. Since the S(CN)$_2$ was not actively pumped through the oven, its transit time through the heated zone was considerably longer than it had been during the previous experiments at The Ohio State University. Eventually, the cell filled to 127 mTorr, but the spectra obtained from the pyrolyzed sample showed no sign of NCNCS; however, strong spectra of NCCN, HNCO, and HNCS were observed. After this disappointment, we considered the calculated relative intensities of the various NCNCS fundamentals (see **Table I**). The ν_7 bending mode at about 80 to 90 cm^{-1} was our chief target, but was predicted to produce a very weak infrared spectrum. We decided to switch the cell windows to KBr and to employ a nitrogen-cooled HgCdTe (Mercury Cadmium Telluride, MCT) detector so that we could observe the two fundamental bands of highest wavenumber, the ν_1 and ν_2 stretching modes between 2000 and 2400 cm^{-1} since they were calculated to be very strong. If we could observe these features, they could be used to optimize production of NCNCS. To this end the pyrolysis oven was set up as shown in steps 5 and 6 of **Fig. 20** so that the S(CN)$_2$ sample could be drawn more rapidly through the hot zone with a high-throughput turbo-molecular pump. We used one cold trap (instead of the two shown in the figure) filled with liquid nitrogen to trap the pyrolysis

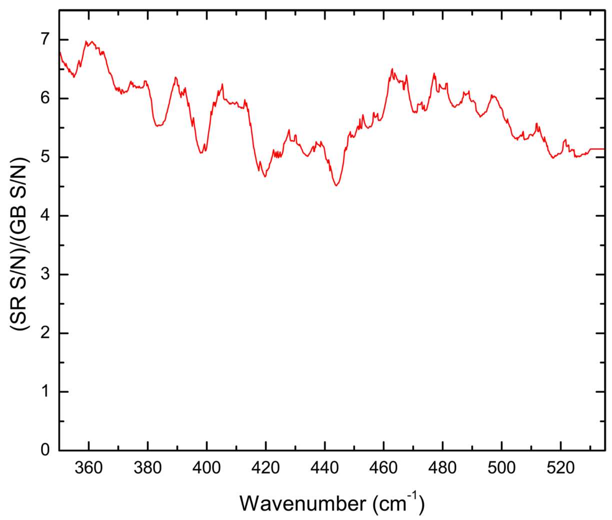

FIG. 18: Ratio of the signal-to-noise achieved using the synchrotron as a source over that achieved using a Globar in the 335 to 535 cm^{-1} region. Both spectra were collected at a nominal resolution of 0.00096 cm^{-1}, with a 1.5 mm aperture, a velocity of 40 kHz, a 6 micron mylar beamsplitter, a liquid helium cooled Cu:Ge detector, a 315-545 cm^{-1} band pass filter and a gain of 4×. Data for both the Globar and the synchrotron were averages of 20 scans. See text for details.

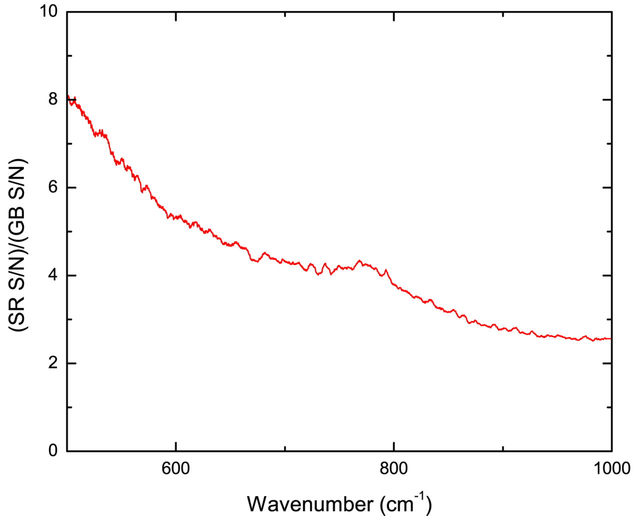

FIG. 19: Ratio of the signal-to-noise achieved using the synchrotron as a source over that achieved using a Globar in the 500 to 1000 cm^{-1} region. Both spectra were collected at a nominal resolution of 0.00096 cm^{-1}, with a 1.3 mm aperture, a velocity of 40 kHz, a KBr beamsplitter, a liquid helium cooled Cu:Ge detector, a 490-1190 cm^{-1} band pass filter and a gain of 4×. Data for both the Globar and the synchrotron were averages of 18 scans. See text for details.

products for later admission into the White cell. We first recorded the spectrum with the cell filled with 185 mTorr of unpyrolized $S(CN)_2$, since its C-N stretching modes were calculated to lie in the same spectral region [18] as those of NCNCS. Indeed, two strong features near 2017 and 2260 cm^{-1} appeared, along with spectra from CO_2 and HNCO. We then evacuate the White cell, and refilled it by warming the pyrolized sample to about $-5\,^\circ$C. To our great surprise, the same two strong features appeared, but much more strongly; only about 7 mTorr of gas was required to see spectra of comparable strength to those of the unpyrolized sample with $S(CN)_2$ sample pressure of 185 mTorr! We collected a high-resolution (0.002 cm^{-1}) spectrum from this sample to conclude our first campaign, believing that we had been unsuccessful at obtaining any spectrum of NCNCS.

5.2 Second measuring campaign May/June 2012 at the CLS: Spectra of $S(CN)_2$ and NCNCS

When we resumed the experiment in May 2012, we decided to improve the quality of the data we had taken the previous year on the stretching modes at 2020 cm^{-1} and 2260 cm^{-1}, and accordingly we admitted 185 mTorr of $S(CN)_2$ vapor into the cooled cell. Building on our experience of the previous year, we were able to produce a much purer sample of $S(CN)_2$, taking particular pains to eliminate any exposure to water vapor in the atmosphere. The sample was left overnight while spectra at 0.0024 cm^{-1} resolution were obtained using a Globar as a background continuum.

The next morning, we found to our great surprise that the spectra of the stretching modes had become progressively more intense over the 14 hour data collection period, and were now saturated, although the pressure of the sample had remained constant! We then ran a controlled test, admitting a fresh 185 mTorr sample of $S(CN)_2$ into the cell and monitoring the change in intensity in the stretching bands with time. Over a period of about 1.5 hours, the intensity of the stretching bands grew steadily. Clearly, the $S(CN)_2$ was converting to another compound, and it was this compound that produced the two bands we were observing.

We realized that the most logical explanation for the observations was that, contrary to our initial assumptions, NCNCS, not $S(CN)_2$, was the more stable isomer, and that the pyrolysis that converted $S(CN)_2$ to NCNCS was required to overcome an internal energy barrier between the two forms, instead of being required to energetically elevate $S(CN)_2$ into the NCNCS form. This idea had, in fact, been very briefly discussed in a paper by King and Kroto in 1984 [53]. What we were observing was the spontaneous conversion of $S(CN)_2$ as it slowly relaxed at room temperature into its more stable form, NCNCS, through intermolecular collisions or collisions with the cell walls. Indeed, according to our most recent *ab initio* calculations [19], NCNCS is about 50 kJ/mol in energy below S(CN)2 .

To confirm our hypothesis, we made a preliminary rotational analysis of the 2017 cm^{-1} band, ν_2 (see **Fig. 21**), first by identification of branches with common values of K_a using a Loomis-Wood [49–51] program written for the software package Igor Pro [52], and then by assigning the R and P branches of the $v_2 = 1 \leftarrow 0$, $K_a = 0$ subband with the lower-state combination differences available from the previous millimeter wave work (see **Table II**). The agreement in combination differences and effective B-values is excellent, given the full width at half maximum (FWHM) widths of about 0.003 cm^{-1} for well-resolved lines in the 2017 cm^{-1} band.

We were now able to exploit the results from the end of the 2011 campaign, which in hindsight demonstrated that NCNCS produced by pyrolysis of $S(CN)_2$ could in fact be trapped and stored under liquid nitrogen. NCNCS prepared as described in subsection 5.1 was then admitted into the White cell at various pressures, and spectra were acquired of the ν_3, ν_5, and ν_8 fundamentals at 1185, 481, and 445 cm^{-1}, and of the $2\nu_8$ band at 890 cm^{-1}. (Details are provided in the captions to **Fig. 21 to 25**, in which the data are displayed.) All bands were consistent in position and intensity with the *ab-initio* calculations given in **Table I** and Ref. [12]. Significant contamination by NCCN, HNCS, HNCO, and CO_2 was observed, but did not greatly interfere with the data we obtained.

We verified that some of our new data were indeed

Step 1

ClSSCl + Cl_2 = 2 SCl_2

Step 2

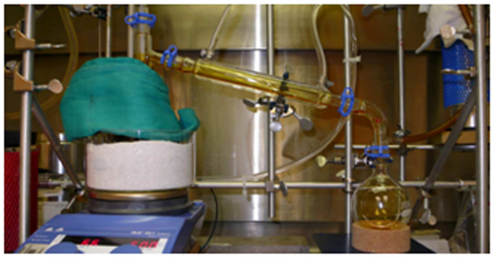

Separation of SCl_2 from ClSSCl by distillation

Step 3

SCl_2 + 2 AgCN = $S(CN)_2$ + 2 AgCl

Step 4

Purification of $S(CN)_2$ by sublimation

Step 5

Thermolysis of $S(CN)_2$ at 750 °C

Step 6

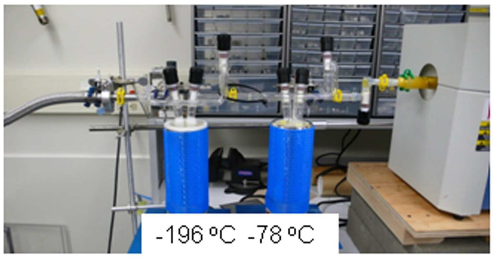

-196 °C
NCCN
HNCO

-78 °C
NCNCS
$S(CN)_2$
HNCS

Fractional trapping of pyrolysis products

FIG. 20: The various steps in the synthesis and purification of NCNCS are depicted. Essentially all the chemical glass and hardware was shipped to the CLS and the syntheses were carried out in the wet chemistry laboratory there.

TABLE II: Confirmation of the first assignment of the NCNCS ν_2 fundamental: $v_2 = 1 \leftarrow 0$, $K_\mathrm{a} = 0$ sub-band via lower state combination differences CD$''$ of the form CD$'' = [R(J-1)] - [P(J+1)] \approx B''_\mathrm{eff}(J+1)(J+2) - B''_\mathrm{eff}(J-1)J = 4B''_\mathrm{eff}(J+\frac{1}{2})$.

J	$R(J)_\mathrm{obs}$ /cm^{-1}	$P(J)_\mathrm{obs}$ /cm^{-1}	CD$''_\mathrm{obs}$ /cm^{-1}	CD$''_\mathrm{cal}$ [a] /cm^{-1}	Δ CD$''_\mathrm{obs-cal}$ /cm^{-1}	B''_eff [b] /cm^{-1}	B''_eff [b] /MHz
10	2017.2121						
11	2017.3249	2014.8411	2.4748	2.4761	**−0.0013**	0.0538000	1612.8987
12	2017.4382	2014.7373	2.6910	2.6913	**−0.0003**	0.0538201	1613.5007
13	2017.5510	2014.6339	2.9059	2.9066	**−0.0007**	0.0538134	1613.2996
14	2017.6644	2014.5323	3.1217	3.1218	**−0.0001**	0.0538223	1613.5672
15	2017.7785	2014.4294	3.3366	3.3370	**−0.0004**	0.0538163	1613.3882
16	2017.8931	2014.3278	3.5511	3.5522	**−0.0011**	0.0538039	1613.0170
17	2018.0077	2014.2275	3.7663	3.7674	**−0.0011**	0.0538047	1613.0407
18	2018.1234	2014.1268	3.9816	3.9826	**−0.0010**	0.0538051	1613.0533
19	2018.2384	2014.0261	4.1975	4.1977	**−0.0002**	0.0538142	1613.3248
20	2018.3547	2013.9259					

[a] The calculated lower state combination differences were obtained from the fitted millimeter wave data presented in Ref. [2].

[b] The infrared B''_eff values are consistent with those for the ground state $v_\mathrm{b} = 0$ for $K_\mathrm{a} = 0$ levels calculated from fitted millimeter wave data presented in Table 3 of the supplementary material of Ref. [2]. Note: B''_eff is the leading term in the power series expansion in $J(J+1)$ in Ref. [2].

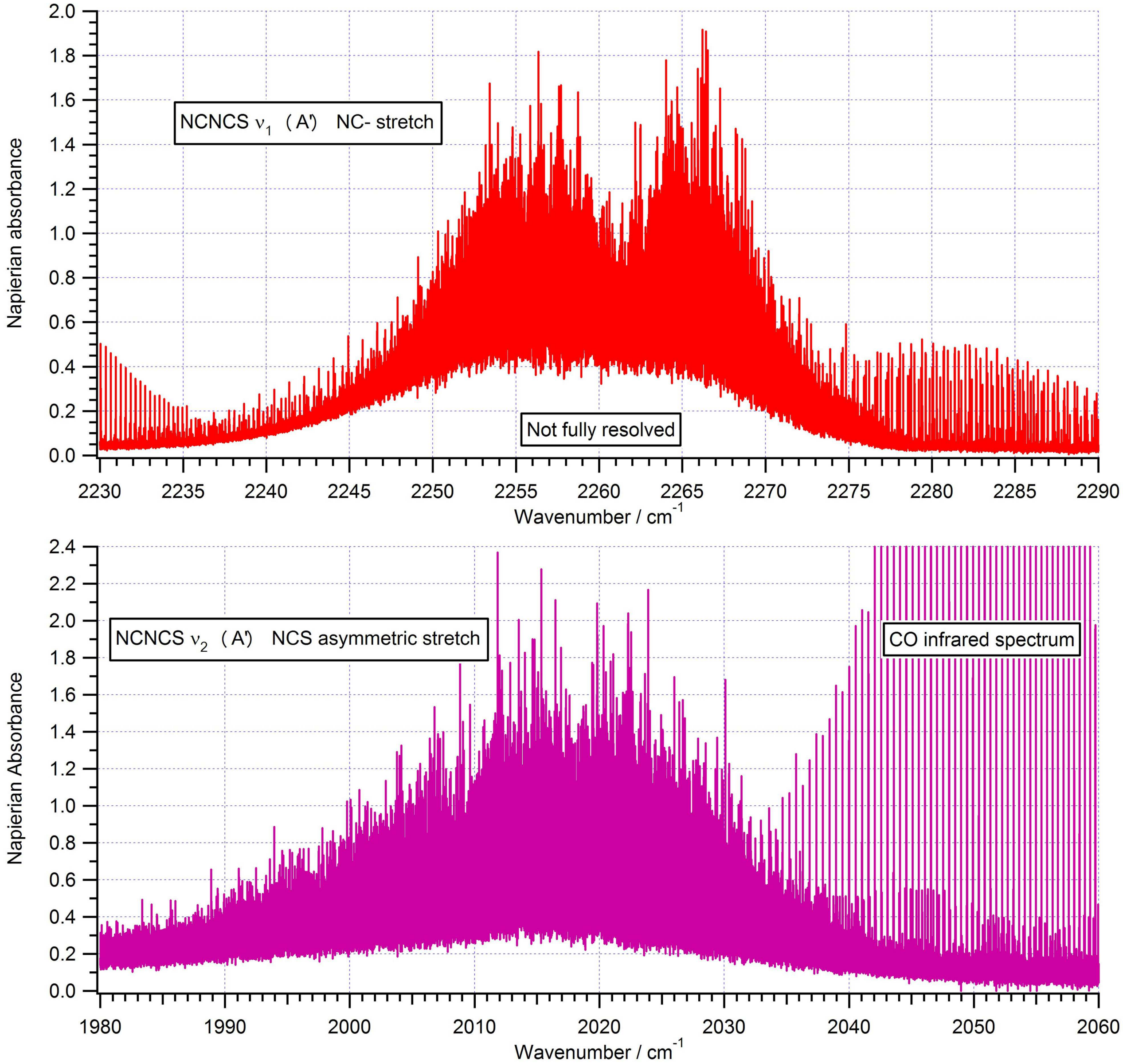

FIG. 21: For this first spectrum (second CLS campaign) of the ν_1 and ν_2 band systems of NCNCS the vapor of $S(CN)_2$ was drawn through the pyrolysis zone at a temperature of 855 °C and trapped under liquid nitrogen and later released into the 2m White cell at a reservoir temperature of -5 °C. The radiation source was a Globar and the detection of the interferograms was achieved with a HgCdTe (Mercury Cadmium Telluride, MCT) detector. for the ν_1 spectrum, about 16 mTorr of gas was admitted into the cell, and 380 interferograms were averaged. For the ν_2 spectrum, only 2 mTorr of gas was used, and 96 interferograms were averaged. In both cases, the Globar (or synchrotron) beam had a path length of 72 m through the cell.

spectra of NCNCS by examining the region of the ν_5 fundamental band, which our calculations place at 472 cm^{-1}. The Loomis-Wood plot quickly revealed a number of strong branches, including two that appeared to be related R and P branches. Both branches exhibited similar local perturbations at the same distance from a common origin at approximately 475.3 cm^{-1}, as shown in **Fig. 25**. We assumed that the perturbation occurred in the upper state, and exploited it to establish a rotational numbering in each branch. When we calculated lower state combination differences they once again were an excellent match to combination differences for the $K_\text{a} = 0$ levels of the ground vibrational state of NCNCS, as is demonstrated in **Table III**, confirming that the band belonged to NCNCS and strongly suggesting that the assigned branches belonged to the ν_5 band.

As the 2012 campaign drew to a close, we directed our attention once again to the ν_7 fundamental band near

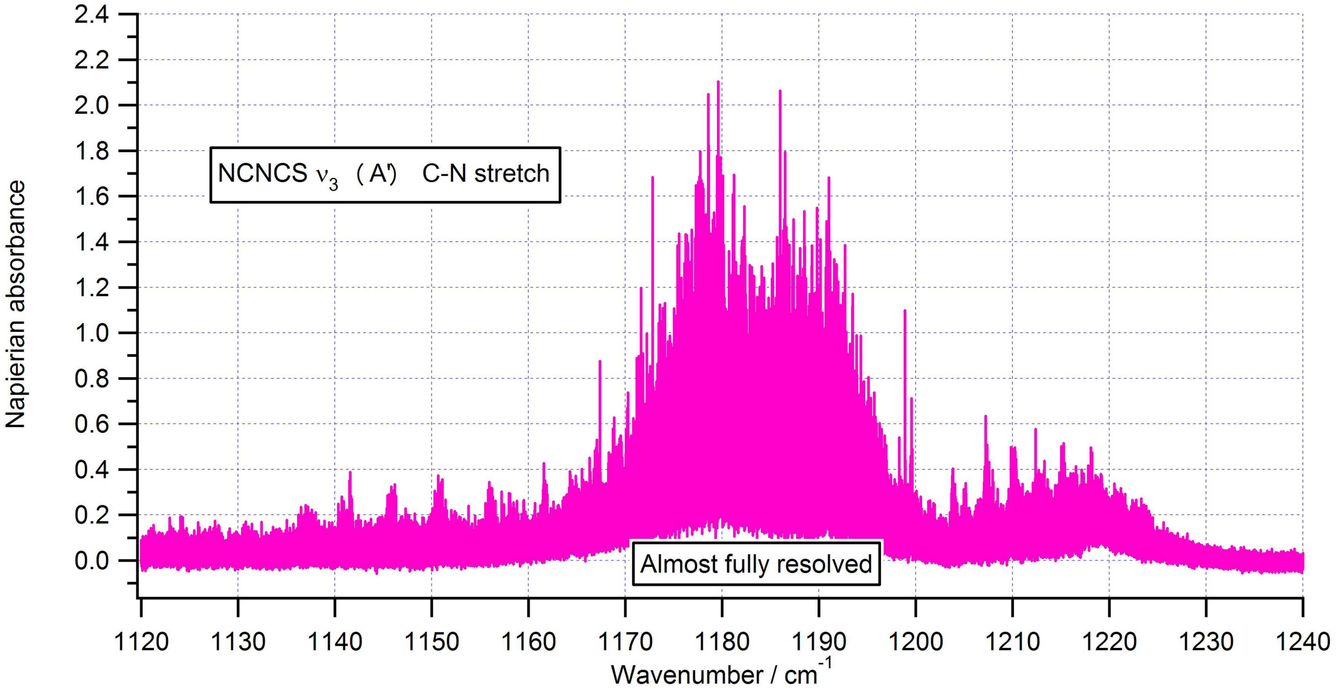

FIG. 22: The high-resolution spectrum of the NCNCS ν_3 band system is almost fully resolved. The measuring parameters are: radiation source Globar; detector: HgCdTe (Mercury Cadmium Telluride, MCT); absorption path 72 m; sample pressure: 42 mTorr; number of co-added interferograms: 82.

80-90 cm^{-1}. After the appropriate windows, beamsplitter and detector were set up, and with the synchrotron used as the light source, we emptied the contents of the last pyrolyzed sample into the cell. We attempted a partial purification by pumping the sample while it was held at dry ice temperature, hoping to remove some of the contaminants previously observed. Over 300 mTorr of gas was admitted into the White cell, and while significant contamination from NCCN was observed, as well as the ν_4 band of $S(CN)_2$ at 135 cm^{-1} [19], an obvious broad spectrum began to emerge at 70-120 cm^{-1}, just where we expected the spectrum we were seeking from NCNCS. We would need to conduct further experiments at the CLS to build on this promising and tantalizing result.

5.3 Third measuring campaign May/June 2013 at the CLS: $S(CN)_2$ and NCNCS

Our previous two campaigns had given us the necessary experience and background information to make the best possible attempt to take the spectrum of the ν_7 bending fundamental of NCNCS and its sequence of associated hot bands. We knew how to grow crystals of the precursor $S(CN)_2$ with high yield and minimum contamination, we knew how to set up pyrolysis of the $S(CN)_2$ to convert it to NCNCS (and trap it), and we knew some rudimentary procedures for extracting the NCNCS from the pyrolyzed and trapped sample. Given the expected weakness (intensity: 4 km/mol) of the band we were seeking, the question remained: could we produce sufficient quantities of NCNCS at acceptable levels of purity to observe the spectrum of interest?

Since we had confidence in our method for synthesizing $S(CN)_2$, we doubled the quantity of chemicals used in the preparation. The resulting $S(CN)_2$ crystals were purified by careful (and slow) sublimation once the liquid in which they were suspended was pumped away. The crystals were held under dry ice until they were required for pyrolysis, at which point they were transferred to a methanol bath at $-15\,^\circ$C (shown at the far right in step 5 of **Fig. 20**), a temperature at which their degradation due to polymerization was very slow. In these runs, two cold traps were employed (see step 6 of **Fig. 20**), the first (a liquid-nitrogen-chilled methanol bath) held between -90 and $-75\,^\circ$C, designed to trap NCNCS and products exiting the pyrolysis tube with a comparable freezing point, and a second held under liquid nitrogen, to trap unwanted impurities like NCCN and CS_2 before they were drawn through the pump that evacuated the entire pyrolysis line. Bypass valves allowed us to isolate each trap separately while pumping in the rest of the chain. The pyrolysis oven was run at $750\,^\circ$C, a compromise between the temperature recommended by King and Kroto [53] and the temperature used in the experiments con-

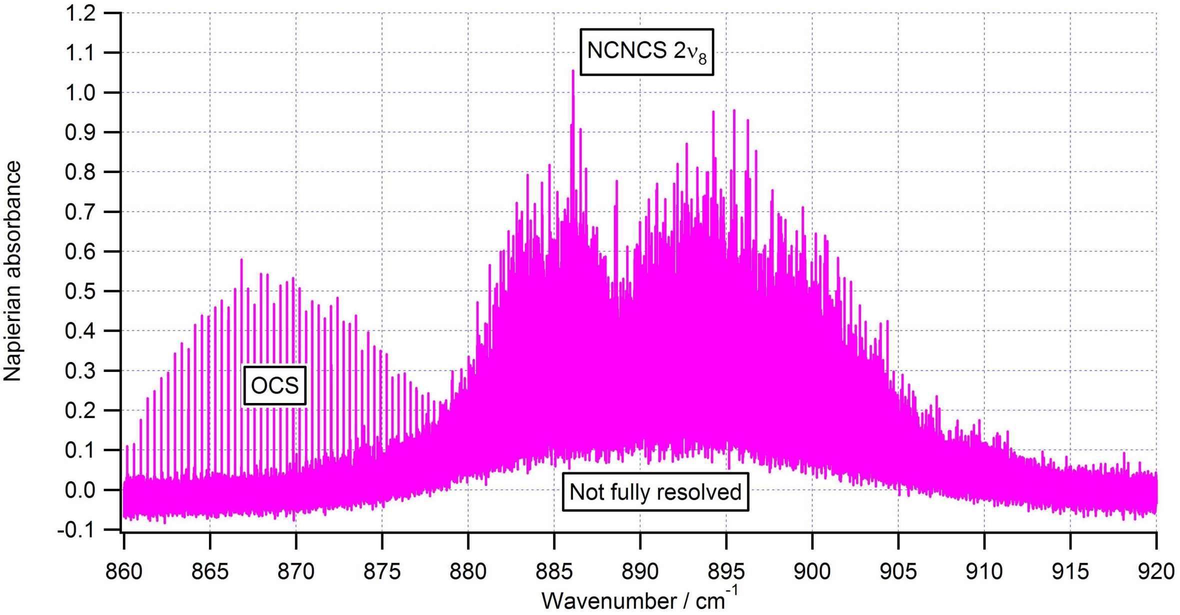

FIG. 23: This spectrum from the second CLS campaign is tentatively assigned to the $2\nu_8$ band [12] of NCNCS, but definitive proof awaits a detailed analysis. The spectrum was obtained with the MCT detector and a Globar as radiation source. The sample pressure was 42 mTorr. The number co-added interferograms was 82 and the absorption path length was 72 m.

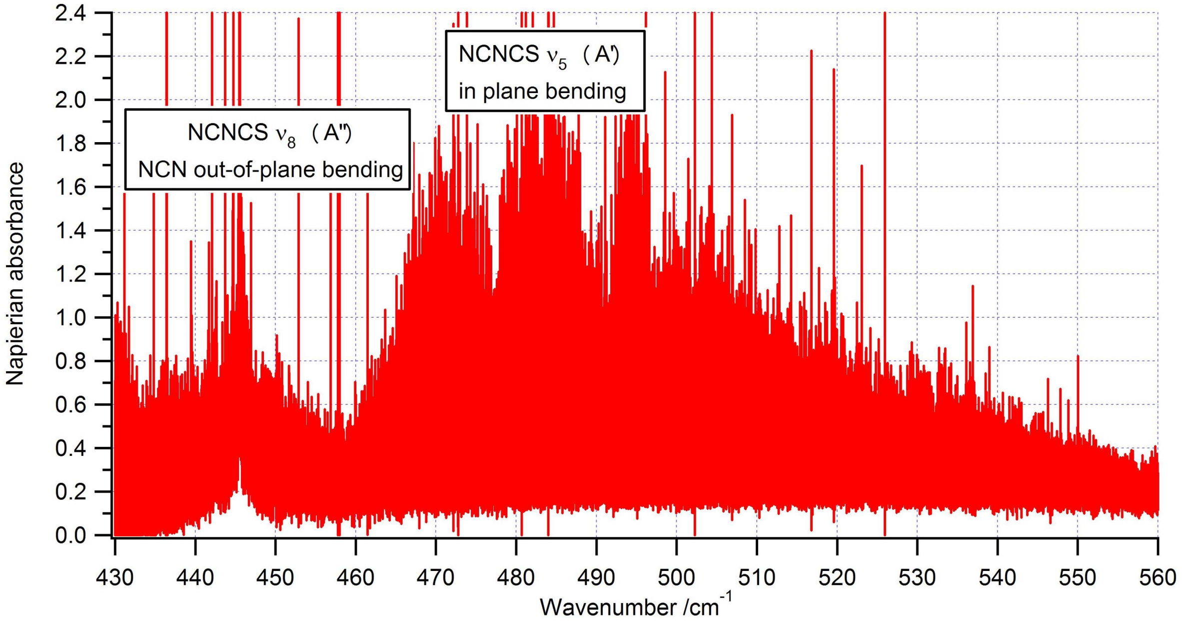

FIG. 24: The spectrum of NCNCS from 430 to 560 cm^{-1} taken during the second CLS campaign contains 4 rather weak fundamental bands of NCNCS (see **Table I**) together with their respective hot-band structures. According to **Fig. 18** the synchrotron has the highest FIR radiation intensity in this region and therefore gives the best signal-to-noise ratio here. The spectrum was taken with the Ge:Cu detector through a filter with a bandwidth extending from of 400 to 750 cm^{-1}. Only 12 mTorr of NCNCS gas was in the cell, so the spectrum is actually very strong, despite the calculations that suggest that these bands would be weak. The assignment of the absorption feature at 445 cm^{-1} to ν_8 follows Ref. [12]. However, according to **Table I**, it may be more likely ν_6 instead, given the calculated position and intensity.

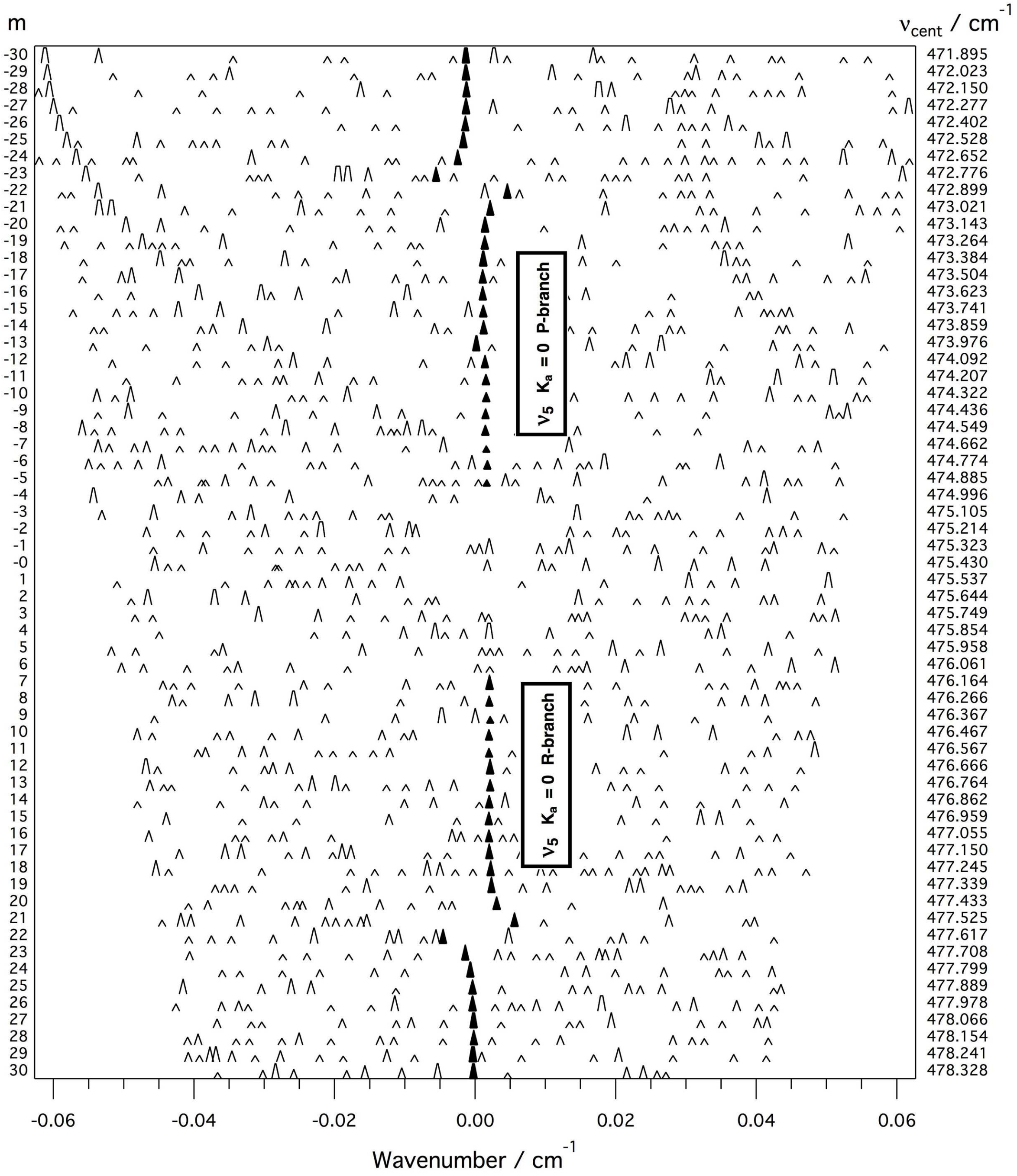

FIG. 25: The high-resolution spectrum of the NCNCS ν_5 band system is fully resolved therefore the Loomis-Wood strands can be found easily. The present tentative assignment is indicated on the graph. The wavenumber indicators on the right side are correct for the center of each row of the Loomis-Wood diagram. The index $m = J + 1$ for the R branch and $m = -J$ for the P branch.

ducted at The Ohio State University. The methanol bath was warmed to about −3 °C, at which point a steady-state pressure of about 120 mTorr of $S(CN)_2$ was produced while pumping. The system was allowed to accumulate NCNCS in the first cold trap for times of between two and six hours, but in principle could have been longer since a fresh sample was not exhausted after even the longest accumulation times. The double trap ensured that many of the species that were previously observed as impurities in our sample were separated from the NCNCS.

After accumulation, we attached the first cold trap to the inlet of the White cell (cooled for these runs to 0 °C), slowly warmed the methanol bath and monitored

TABLE III: Confirmation of the first assignment of the NCNCS ν_5 sub-band $v_5 = 1 \leftarrow 0$, $v_\mathrm{b} = 0$, $K_\mathrm{a} = 0$ via lower state combination differences CD$''$ of the form CD$'' = [R(J-1)] - [P(J+1)] \approx B''_\mathrm{eff}(J+1)(J+2) - B''_\mathrm{eff}(J-1)J = 4B''_\mathrm{eff}(J+\frac{1}{2})$.

J	$R(J)_\mathrm{obs}$ /cm^{-1}	$P(J)_\mathrm{obs}$ /cm^{-1}	CD$''_\mathrm{obs}$ /cm^{-1}	CD$''_\mathrm{cal}$ ^{a} /cm^{-1}	Δ CD$''_\mathrm{obs-cal}$ /cm^{-1}	B''_eff ^{b} /cm^{-1}	B''_eff ^{b} /MHz	B'_eff ^{c} /MHz
7	476.26764	474.66364	1.61490	1.61490	**±0.00000**	0.053830	1613.78680	1602.87420
8	476.36894	474.55088	1.83007	1.83020	**−0.00013**	0.053826	1613.64878	1603.04943
9	476.46923	474.43757	2.04531	2.04550	**−0.00019**	0.053824	1613.60135	1602.81619
10	476.56896	474.32363	2.26040	2.26080	**−0.00040**	0.053819	1613.45089	1602.68376
11	476.66815	474.20883	2.47572	2.47610	**−0.00038**	0.053820	1613.48040	1602.77901
12	476.76647	474.09325	2.69229	2.69130	**+0.00099**	0.053846	1614.25767	1602.81165
13	476.86393	473.97586	2.90643	2.90660	**−0.00017**	0.053823	1613.56906	1603.36186
14	476.96076	473.86003	3.12152	3.12180	**−0.00028**	0.053819	1613.46233	1602.70112
15	477.05696	473.74241	3.33668	3.33700	**−0.00032**	0.053817	1613.40758	1602.69426
16	477.15246	473.62408	3.55185	3.55220	**−0.00035**	0.053816	1613.35900	1602.68870
17	477.24741	473.50512	3.76693	3.76740	**−0.00047**	0.053813	1613.28300	1602.71717
18	477.34157	473.38553	3.98202	3.98260	**−0.00058**	0.053811	1613.21482	1602.67937
19	477.43566	473.26539	4.19718	4.19770	**−0.00052**	0.053810	1613.18399	1602.82608
20	477.53084	473.14439	4.41227			0.053808	1613.12728	1603.67542
21	477.61261	473.02339	4.62743			0.053807	1613.10304	1599.76833
22	477.70701	472.90341	4.84244			0.053805	1613.02866	1600.07716
23	477.79827	472.77017	5.05752			0.053803	1612.98612	1603.58819
24	477.88843	472.64948	5.27245			0.053801	1612.89903	1602.63574

[a] The calculated lower state combination differences were obtained from the fitted millimeter wave data presented in Ref. [2].

[b] The infrared B''_eff values are consistent with those for the ground state $v_\mathrm{b} = 0$ for $K_\mathrm{a} = 0$ levels calculated from fitted millimeter wave data presented in Table 3 of the supplementary material of Ref. [2].

[c] The upper state combination differences yield the infrared B'_eff values which can at present only tentatively be assigned to ν_5.

TABLE IV: Confirmation of the assignment of the NCNCS ν_7 sub-band $v_\mathrm{b} = 3 \leftarrow 2$, $K_\mathrm{a} = 0$ via combination differences for the upper state CD$'$ and lower state CD$''$. P and R transitions are also compared with the GSRB predicted values from Ref. [2]. All numerical entries except the rotational quantum number J are in units of cm^{-1}.

J	$P(J)_\mathrm{obs}$	$P(J)_\mathrm{obs} - P(J)_\mathrm{cal}$	$R(J)_\mathrm{obs}$	$R(J)_\mathrm{obs} - R(J)_\mathrm{cal}$	CD$'_\mathrm{obs}$	CD$'_\mathrm{obs}$ − CD$'_\mathrm{cal}$ ^{a}	CD$''_\mathrm{obs}$	CD$''_\mathrm{obs}$ − CD$''_\mathrm{cal}$ ^{a}
09								
10	68.60729	0.37351						
11	68.49666	0.37320	70.94836	0.37406	2.45170	**+0.00084**		
12	68.38664	0.37383	71.05121	0.37446	2.66457	**+0.00063**	2.67250	**+0.00005**
13	68.27586	0.37402	71.15362	0.37476	2.87776	**+0.00074**	2.88626	**+0.00006**
14	68.16495	0.37440	71.25560	0.37494	3.09065	**+0.00054**	3.10042	**+0.00004**
15	68.05321	0.37427	71.35708	0.37496	3.30387	**−0.00069**	3.31363	**−0.00001**
16	67.94197	0.37495	71.45830	0.37503	3.51633	**−0.00008**	3.52729	**−0.00004**
17	67.82979	0.37500	71.55994	0.37583	3.73015	**−0.00083**		
18	67.71773		71.66068					

[a] The calculated upper and lower state combination differences [defined as: CD $= R(J-1) - P(J+1)$] and with neglecting centrifugal distortion [CD$' \approx 4B'_\mathrm{eff}(J+\frac{1}{2})$] and [CD$'' \approx 4B''_\mathrm{eff}(J+\frac{1}{2})$] were obtained from the fitted millimeter wave data presented in Table 3 of the supplementary material of Ref. [2].

the spectrum of vapor reaching the cell. At temperatures between −45 °C and −25 °C, sample vapors evolved from the trap; if the temperature was allowed to rise to near 0 °C, significantly more gas evolved, subsequently shown to be HNCS and residual S(CN)$_2$ trapped with the NCNCS. Accordingly, the cell was then evacuated and filled with progressively higher pressures of the gas evolving below −25 °C range. In the earliest run we produced only 35 mTorr of sample, but in the final experiment we were able to fill the cell to 121 mTorr. To our delight, each spectrum showed progressively stronger signal consistent with our observations from the end of the second campaign. The ν_7 far-infrared spectrum of NCNCS is shown in **Fig. 26** together with the predicted a-type stick spec-

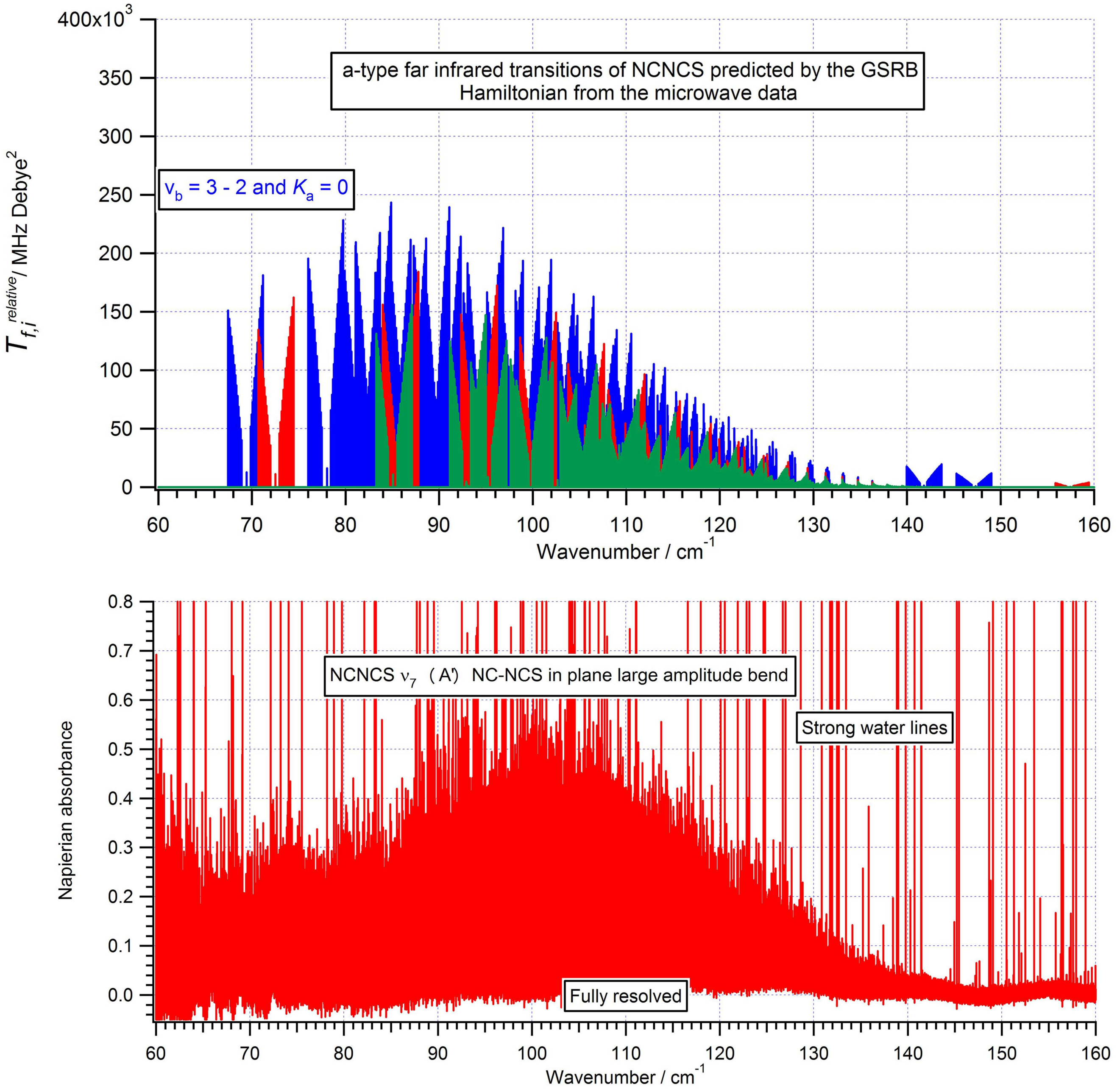

FIG. 26: The top panel displays a truncated stick-spectrum of the GSRB calculated sub-bands of the ν_7 large amplitude bending mode of NCNCS [2, 13]. Calculations predict both a-type and b-type bands, but only a-type transitions have been definitively assigned in the spectrum so far obtained from our third CLS campaign (bottom panel). The assignment is confirmed via the combination difference matches presented in **Table IV**. Note that the R-branch extends to $J > 80$ while the P-branch is observed only to $J = 37$ due to the limits of detection in the low-wavenumber region (excessive noise).

trum with truncated sub-bands. As can be seen from **Fig. 26** and **Fig. 27** the experimental ν_7 FIR spectrum is essentially fully resolved. The bottom of the band system stays close to 0 Napierian absorbance.

P- and R-branches (see **Fig. 28**) were easily identified with the aid of the Loomis-Wood program, and by using combination differences from the previously analyzed millimeter-wave rotational spectra [2] we soon identified a-type transitions from several sub-bands of the ν_7 sequence of NCNCS: $K_\mathrm{a} = 0$ and $v_\mathrm{b} = 1 \leftarrow 0,\ 2 \leftarrow 1,\ 3 \leftarrow 2$; $K_\mathrm{a} = 1$ and $v_\mathrm{b} = 1 \leftarrow 0,\ 2 \leftarrow 1,\ 3 \leftarrow 2$; and $K_\mathrm{a} = 2$ and $v_\mathrm{b} = 1 \leftarrow 0$ (see **Fig. 29**).

The first assignment was carried out on the lowest-wavenumber end of the recorded spectrum by finding the

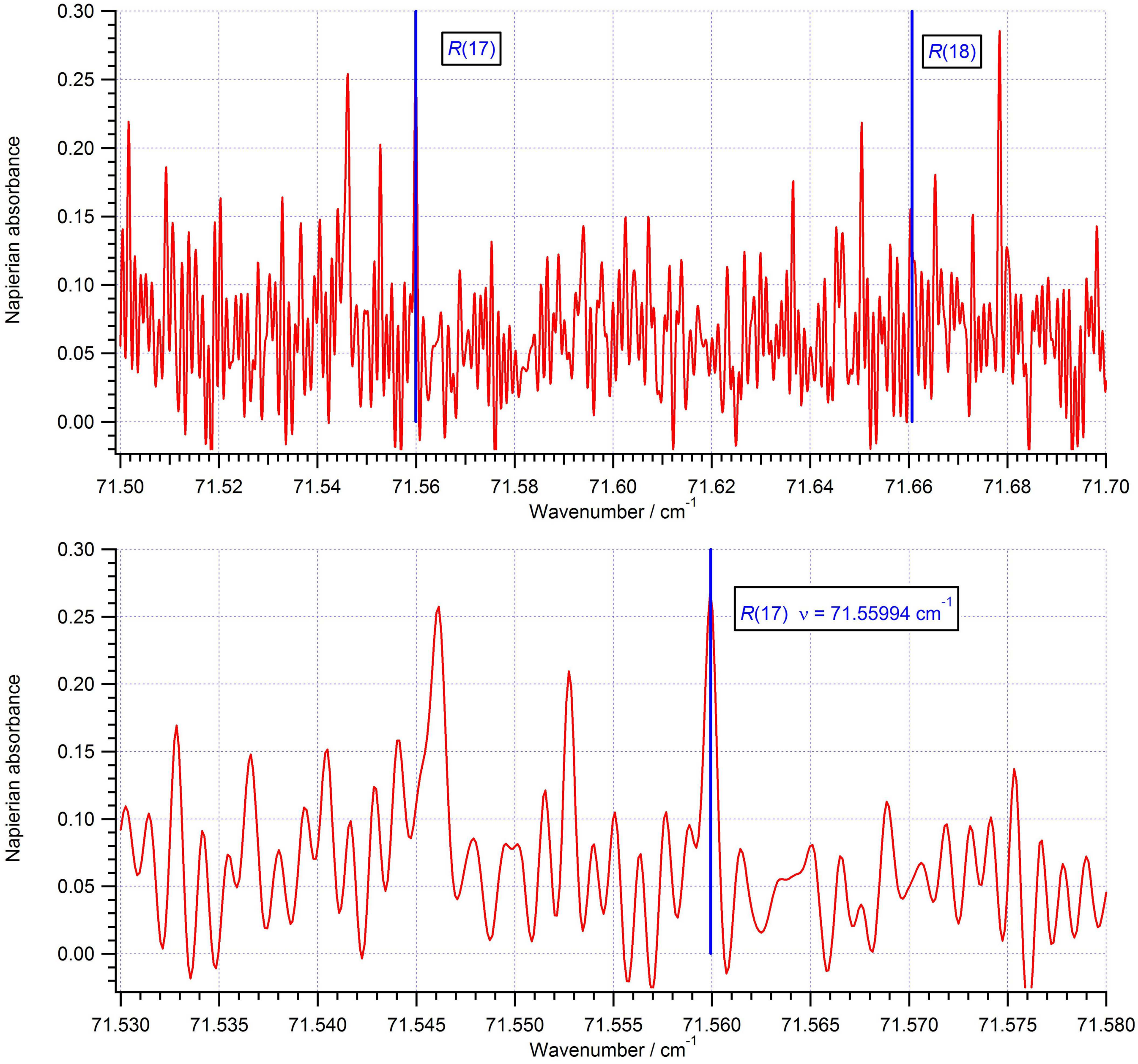

FIG. 27: The ν_7 large amplitude in-plane bending spectrum of NCNCS is clearly resolved in this spectrum from the third CLS campaign. Two a-type R branch transitions are identified and were found by the application of the Loomis-Wood procedure which is illustrated in **Fig. 28**. The lower panel zooms in on the $R(17)$ transition. The application of the Loomis-Wood procedure [49–52] in high-resolution Fourier transform spectra is of great help in identifying strands of absorption lines which belong to series of adjacent rotational lines with different J values; the random noise features which also look like lines do not form strands.

P- and R-branches of the $K_\mathrm{a} = 0$ $v_\mathrm{b} = 3 \leftarrow 2$ sub-band. As shown in **Table IV**, the assignments, confirmed via upper and lower state combination differences, left no doubt that we had succeeded in obtaining the spectrum we sought. **Figure 27** shows a close view of two assigned lines, demonstrating that they are very well resolved. The full width at half maximum for these lines is about 0.00088 cm^{-1}.

Curiously, while calculations predict that both a- and b-type transitions of comparable intensity should be observed as indicated in **Fig. 11**, we have so far observed only a-type transitions. At the time of writing we have identified 48 Loomis-Wood strands, corresponding to 24 sub-bands with P and R branches, and many more sub-

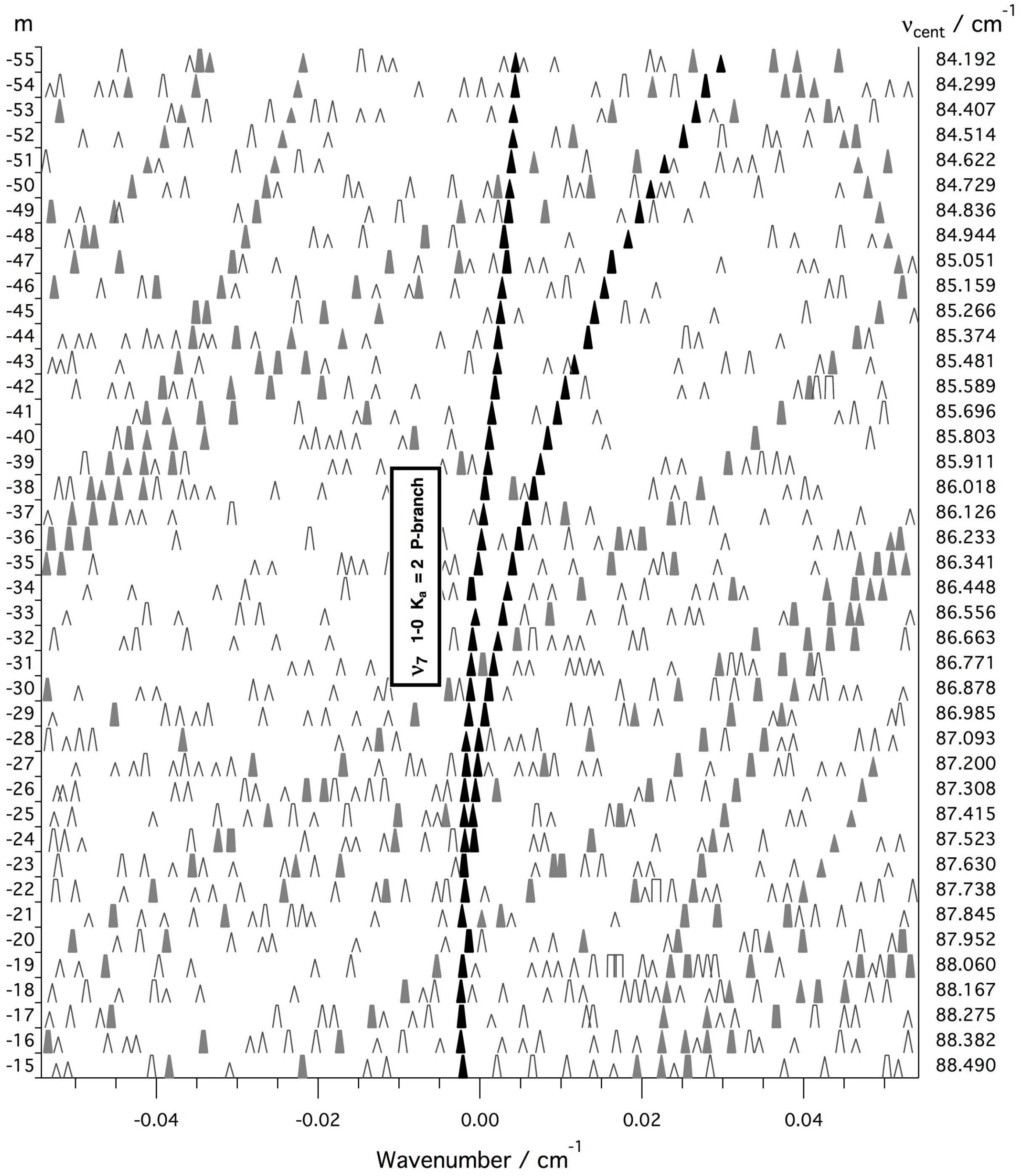

FIG. 28: Excerpt from the Loomis-Wood diagrams that enable us to assign branches of sub-bands of the ν_7 a-type band system of NCNCS. The ν_7, $v_\mathrm{b} = 1 \leftarrow 0$, $K_\mathrm{a} = 2$ P-branch is indicated in black, and shows a prominent splitting. The m-index numbering on the left side is correct for this branch, and the index $m = -J$ for the P branch is shown. Other branches, most of which have been assigned, are indicated in gray. The wavenumber indicators on the right side are correct for the center of each row of the Loomis-Wood diagram.

bands remain to be identified and will be assigned.

6. CONCLUSION AND PERSPECTIVE

Our investigation of the effects of quantum monodromy on the spectrum of NCNCS is nearly complete. We have found that this elusive species is more stable than its isomer $S(CN)_2$, in agreement with our recent ab

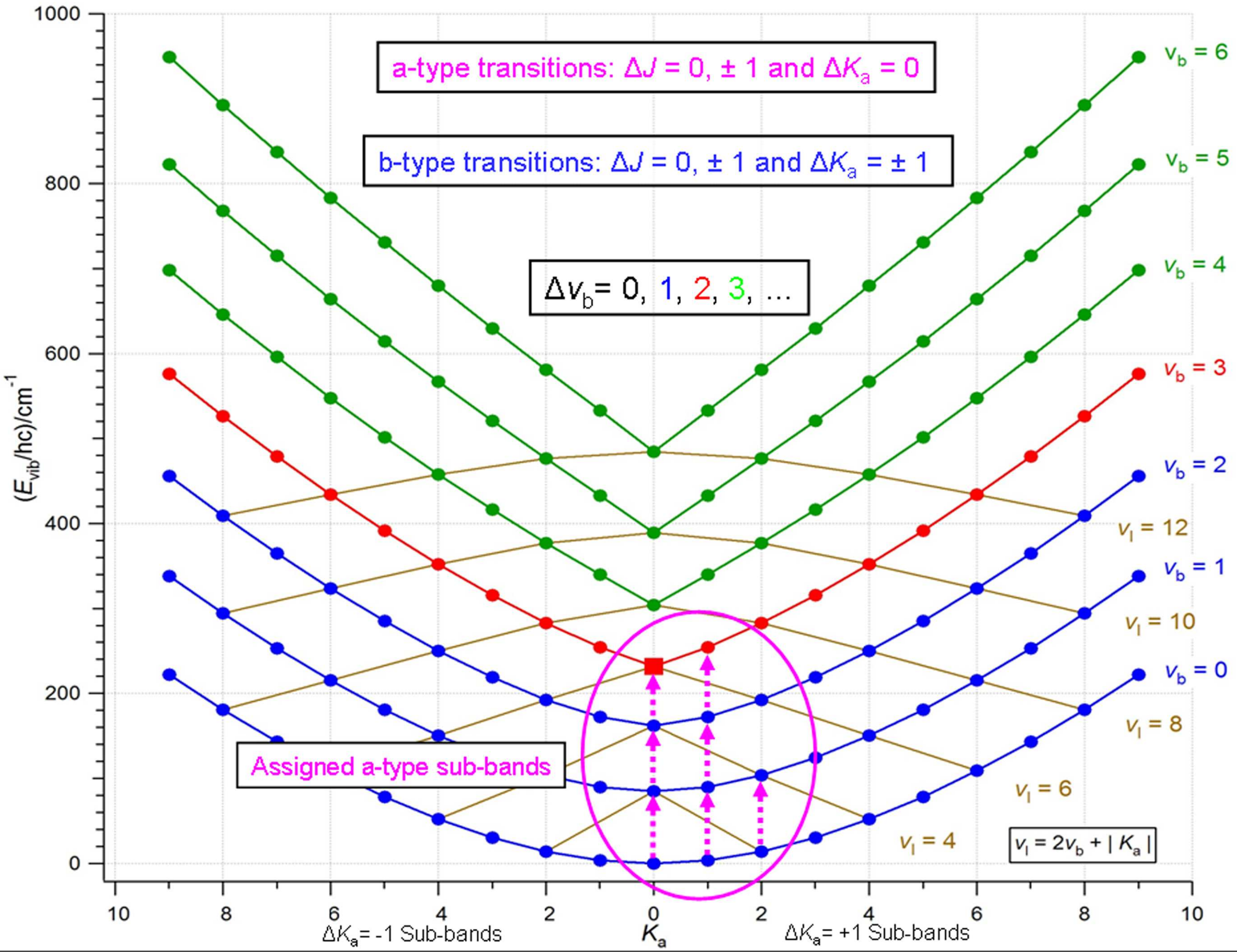

FIG. 29: Excerpt of the energy-momentum map for $J = K_\mathrm{a}$ with the 7 assigned sub-bands of the ν_7 large amplitude in-plane bending mode of NCNCS for $K_\mathrm{a} = 0$ and $v_\mathrm{b} = 1 \leftarrow 0, 2 \leftarrow 1, 3 \leftarrow 2$; for $K_\mathrm{a} = 1$ and $v_\mathrm{b} = 1 \leftarrow 0, 2 \leftarrow 1, 3 \leftarrow 2$; for $K_\mathrm{a} = 2$ and $v_\mathrm{b} = 1 \leftarrow 0$. Please note that in the linear molecule notation v_l stands for v_linear. Through out this paper we have use the notation of a bent molecule with v_b. Both quantum numbers are related to each other as is indicated in this figure. As of this writing 48 Loomis-Wood strands have been identified, allowing us to start building a fully experimental version of the ro-vibration energy-momentum map.

initio calculation which has it more stable by about 50 kJ/mol [19], and that we can produce it reliably and consistently in the requisite quantities at the CLS. Further, we have found that it exhibits remarkable chemical and kinetic stability in a 2-m-long stainless steel White cell if the cell is cooled below 0 °C. In addition to acquiring spectra of several small-amplitude vibrational modes in NCNCS, we have attained our main goal of observing the large-amplitude bending mode ν_7 and its associated sequence bands through its ro-vibrational spectrum near 80 cm^{-1}. Not detailed here, but shown in **Table IV**, is the fact that the GSRB calculations predict the a-type ro-vibrational transitions currently assigned with a discrepancy from observations of no more than 0.375 cm^{-1}; a remarkable result since the calculated spectrum was based only on the analysis of $\Delta v_\mathrm{b} = \Delta K_\mathrm{a} = 0$ pure rotational data [2], that are the transitions leading to the small peak on the extreme left of the bottom panel of **Fig. 11**.

The transitions we have observed are indicated on the energy-momentum map shown in **Fig. 29**. The newly acquired far-infrared spectra allow us to determine for the first time the term values of several excited bending vibrational levels relative to the term value of levels in the ground vibrational state. However, since only a-type transitions have been observed ($\Delta K_\mathrm{a} = 0$), only the levels with a common value of K_a can be placed on an absolute scale with respect to each other. To find the absolute energy of all levels relative to the lowest possible level, transitions with $\Delta K_\mathrm{a} = \pm 1$ must be observed and assigned. The b-type ro-vibrational transitions predicted to be of appreciable intensity in the far-infrared spectrum by the GSRB calculations would be suitable for this purpose, but no evidence for them has been seen in the portion of the spectrum analyzed to date. A similar situation was previously reported in the pure rotational spectra, for which both a- and b-type transitions were predicted to occur, but in which only the a-type transitions have so far been identified [2].

Thus, the question remains: where are the b-type rotational or ro-vibrational transitions (see **Fig. 11**)? Perhaps they are considerably weaker than predicted, and the signal-to-noise ratio of our data is not yet sufficient to reveal them. It is also important to note that the intensities calculated using the GSRB rely on the *ab initio* dipole moment functions of Ref. [2]. Any inaccuracy in those results will be reflected here, particularly strongly given the square in **eqn (5)**.

In May 2014 we will perform a final experiment at the CLS, intending to improve the signal-to-noise ratio of the far-infrared spectrum so that we can answer the question posed above. In the meantime the full analysis of the spectrum already acquired is being carried out, and consideration is also being given to the bands associated with small-amplitude vibrations. If hybrid a-b-type or even a-c-type transitions for out-of-plane vibrations can be observed in the latter spectra, we may be able to meet our objective of building a fully experimental energy-momentum map even if the b-type transitions in the far-infrared spectrum are not observed.

Our GSRB calculations concerning energy levels, line positions, wavefunctions, expectation values of dipole moment components and line intensities together with initial results presented in this work indicate that the unusual structure of the large amplitude bending fundamental band system of NCNCS is a very specific signature of monodromy. Such signatures must appear in the spectrum of any molecule that is excited above its barrier to linearity.

ACKNOWLEDGEMENTS

The experimental work of The Ohio State University team was supported by the Army Research Office, NSF, and NASA. B. Billinghurst would like to thank all of his colleagues at the Canadian Light Source for their advice particularly Dr. J. C. Bergstrom for endless discussions about the physics of synchrotrons. Damien Forthomme and Colin Sonnichsen are thanked for their help with the initial experiments. Dr. Sylvestre Twagirayezu is recognized and thanked for all his help in setting up the chemical laboratory in May 2013. DWT acknowledges financial support from the Natural Sciences and Engineering Research Council of Canada (NSERC). The experimental part of the research described in this paper was performed at the Canadian Light Source, which is funded by the Canada Foundation for Innovation, the Natural Sciences and Engineering Research Council of Canada, the National Research Council Canada, the Canadian Institutes of Health Research, the Government of Saskatchewan, Western Economic Diversification Canada, and the University of Saskatchewan. The authors thank Professor Zbigniew Kisiel for critically reading the manuscript.

[1] D. J. Nesbitt and M. A. Suhm, Phys. Chem. Chem. Phys. **12**, 8151 (2010).

[2] B. P. Winnewisser, M. Winnewisser, I. R. Medvedev, F. C. De Lucia, S. C. Ross, and J. Koput, Phys. Chem. Chem. Phys. **12**, 8158 (2010).

[3] D. Larese and F. Iachello, J. Mol. Structure **1006**, 611 (2011).

[4] D. Larese, F. Perez-Bernal, and F. Iachello, J. Mol. Struct. **1051**, 310 (2013).

[5] L. M. Bates, J. Appl. Math. Phys. (ZAMP) **42**, 837 (1991).

[6] R. Cushman and J. J. Duistermaat, Bull. Am. Math. Soc. **19**, 475 (1988).

[7] M. S. Child, J. Phys. A: Math. Gen. **31**, 657 (1998).

[8] M. S. Child, T. Weston, and J. Tennyson, Mol. Phys. **96**, 371 (1999).

[9] M. S. Child, J. Mol. Spectrosc. **210**, 157 (2001).

[10] B. P. Winnewisser, M. Winnewisser, I. R. Medvedev, M. Behnke, F. C. De Lucia, S. C. Ross, and J. Koput, Phys. Rev. Lett. **95**, 243002 (2005).

[11] M. Winnewisser, B. P. Winnewisser, I. R. Medvedev, F. C. De Lucia, S. C. Ross, and L. M. Bates, J. Mol. Struct. **798**, 1 (2006).

[12] Jin Wang, *Mid-infrared and computational investigations of unstable molecules: The pseudohalide Groups -NCO, -NCS, and P, C, O structural isomers,* Dissertation, University of Guelph (Library and Archives Canada, Published Heritage Branch, 395 Wellington Street, Ottawa ON K1A 0N4, Canada, 2007).

[13] M. A. King, H. W. Kroto, and B. M. Landsberg, J. Mol. Spectrosc. **113**, 1 (1985).

[14] D. T. Petkie, T. M. Goyette, R. P. A. Bettens, S. P. Belov, S. Albert, P. Helminger, and F. C. De Lucia, Rev. Sci. Instum. **68**, 1675 (1997).

[15] I. Medvedev, M. Winnewisser, F. C. De Lucia, E. Herbst, E. Białkowska-Jaworska, L. Pszczółkowski, and Z. Kisiel, J. Mol. Spectrosc. **228**, 314 (2004).

[16] P. Groner, M. Winnewisser, I. R. Medvedev, F. C. De Lucia, E. Herbst, and K. V. L. N. Sastry, Astrophys. J. Suppl. Ser. **169**, 28 (2007).

[17] K. Yamada and M. Winnewisser, Z. Naturforsch. **30a**, 672 (1975).

[18] Z. Kisiel, O. Dorosh, M. Winnewisser, M. Behnke, I. R. Medvedev, and Frank C. De Lucia, J. Mol. Spectrosc. **246**, 39 (2007).

[19] Z. Kisiel, M. Winnewisser, B. P. Winnewisser, F. C. De Lucia, D. W. Tokaryk, and B. E. Billinghurst, J. Phys. Chem. A **117**, 13815 (2013).

[20] P. R. Bunker and J. M. R. Stone, J. Mol. Spectrosc. **41**, 310 (1972).

[21] P. A. M. Dirac, Proc. Roy. Soc. (London) **A 114 (767)**,

243 (1927).
[22] P. R. Bunker and P. Jensen, *Molecular Symmetry and Spectroscopy, Second Edition* (NRC Research Press, Ottawa, Ontario, Canada, 1998).
[23] C. di Lauro and I. M. Mills , J. Mol. Spectrosc. **21**, 386 (1966).
[24] A. R. W. McKellar, J. Mol. Spectrosc. **262**, 1 (2010).
[25] J. C. Pearson, B. J. Drouin, A. Maestrini, I. Mehdi, and J. Ward et al., Rev. Sci. Instrum. **82**, 093105 (2011).
[26] J. C. Pearson, B. J. Drouin, S. Yu, and H. Gupta, J. Opt. Soc. Am. B **28**, 2549 (2011).
[27] R. P. Feynman, R. B. Leighton, and M. Sands, *The Feynman Lectures on Physics* (Addison-Wesley, USA, 1963).
[28] J. D. Jackson, *Classical Electrodynamics* (3^{rd} Edition, Wiley, USA, 1998).
[29] K-J. Kim, *AIP Conf. Proc.* **184***, 565 (1989)* (American Institute of Physics, USA, 1989).
[30] B. D. Patterson, Am. J. Phys. **79**, 1046 (2011).
[31] A. L. Robinson, *X-Ray Data Booklet Section 2.2 History of Synchrotron Radiation (October 10, 2012)* (http://xdb.lbl.gov/Section2/Sec 2-2.html, 2012).
[32] J. P. Blewett, Phys. Rev. **69**, 87 (1946).
[33] F. R. Elder, A. M. Gurewitsch, R. V. Langmuir, and H. C. Pollock, Phys. Rev. **71**, 827 (1947).
[34] G. C. Baldwin and D. W. Kerst, Phys. Today. **28**, 9 (1975).
[35] B. Nelander, J. Mol. Struct. **294**, 205 (1993).
[36] B. Nelander, Vib. Spectrosc. **9**, 29 (1995).
[37] P. Roy, J-B. Brubach, P. Calvani, G. deMarzi, A. Filabozzi, A. Gerchel, P. Giura, S. Lupi, O. Marcouillé, A. Mermet, A. Nucara, J. Orphal, A. Paolone, and M. Vervloet, Nuclear Instruments and Methods in Physics Research, Section A, **467-468**, 426 (2001).
[38] A. R. W. McKellar, D. Tokaryk, L-H. Xu, D. R. T. Appadoo, and T. May, J. Mol. Spectrosc. **241**, 31 (2007).
[39] A. Cuisset, L. Nanobashili, I. Smirnova, R. Bocquet, F. Hindle, G. Mouret O. Pirali, P. Roy, and D. A. Sadovskii, Chem. Phys. Lett. **492**, 30 (2010).
[40] T. Chimdi, E. G. Robertson, L. Puskar, C. D. Thompson, M. J. Tobin, and D. McNaughton, Chem. Phys. Lett. **465**, 203 (2008).
[41] B. Billinghurst and J. C. Bergstrom, Physics in Canada **67**, 17 (2011).
[42] A. Savitzky and M. J. E. Golay, Anal. Chem. **36**, 1627 (1964).
[43] M. A. King and H. W. Kroto, J. Chem. Soc. Chem. Commun. p. 606 (1980).
[44] R. Neidlein and H. G. Reuter, Arch. Pharm. (Weinheim, Germany) **308**, 189 (1978).
[45] T. C. Devore, J. Mol. Structure **162**, 287 (1987).
[46] P. Li, L. K. Keong, and W. Y. Fan , Chem. Phys. Lett. **380**, 117 (2003).
[47] G. Brauer, Editor, *Handbuch der Präparativen Anorganischen Chemie* (Ferdinand Enke Verlag Stuttgart, Germany, 1960).
[48] D. A. Long and D. Steele, Spectrochim. Acta **19**, 1731 (1963).
[49] F. W. Loomis and R. W. Wood, Phys. Rev. **32**, 223 (1928).
[50] B. P. Winnewisser, J. Reinstädtler, K. M. T. Yamada, and J. Behrend, J. Mol. Spectrosc. **132**, 12 (1989).
[51] I. R. Medvedev, M. Winnewisser, B. P. Winnewisser, F. C. De Lucia, and E. Herbst, J. Mol. Structure **742**, 229 (2005).
[52] C. F. Neese, *An interactive Loomis-Wood package for spectral assignment in Igor Pro, version 2.0,* 56th Ohio State University International Symposium on Molecular Spectroscopy (The Ohio State University, Columbus, Ohio, 2001).
[53] M. A. King and H. W. Kroto, J. Am. Chem. Soc. **106**, 7347 (1984).